Sub-daily live fuel moisture content estimation from Himawari-8 Data

Xingwen Quan[a,b*], Rui Chen[a], Marta Yebra[c,d], David Riaño[e,f], Víctor Resco de Dios[g,h,i], Xing Li[j], Binbin He[a], Rachael H. Nolan[k,l], Anne Griebel[m], Matthias M. Boer[k,l], Yuanqi Sun[a]

[a]School of Resources and Environment, University of Electronic Science and Technology of China, Chengdu, Sichuan 611731, China

[b]Yangtze Delta Region Institute (Huzhou), University of Electronic Science and Technology of China, Huzhou 313001, China

[c]Fenner School of Environment and Society, The Australian National University, ACT, Canberra, Australia

[d]School of Engineering, The Australian National University, ACT, Canberra, Australia

[e]Center for Spatial Technologies and Remote Sensing (CSTARS), University of California, 139 Veihmeyer Hall, One Shields Avenue, Davis, CA 95616, USA

[f]Instituto de Economía, Geografía y Demografía (IEGD), Centro de Ciencias Humanas y Sociales (CCHS), Consejo Superior de Investigaciones Científicas (CSIC), Albasanz 26-28, 28037 Madrid, Spain

[g]School of Life Science and Engineering, Southwest University of Science and Technology, Mianyang, China

[h]Department of Crop and Forest Sciences, University of Lleida, Lleida, Spain

[i]Joint Research Unit CTFC-AGROTECNIO, Universitat de Lleida, Lleida, Spain

[j]Research Institute of Agriculture and Life Sciences, Seoul National University, Seoul, South Korea

[k]Hawkesbury Institute for the Environment, Western Sydney University, Locked Bag 1797, Penrith, New South Wales 2751, Australia

[l]NSW Bushfire Risk Management Research Hub, Wollongong, NSW 2522, Australia

[m]School of Life Sciences, University of Technology Sydney, PO Box 123, Broadway, NSW 2007, Australia.

[*] Corresponding author.

E-mail address: xingwen.quan@uestc.edu.cn

Abstract

Live fuel moisture content (LFMC) is a crucial variable affecting fire ignition and spread. Satellite remote sensing has been effective in estimating LFMC over large spatial scales, but continuous sub-daily (e.g., every 10 mins to hourly during daylight) LFMC monitoring from space is yet to be accomplished. Using the geostationary satellite Himawari-8 temporally dense observations every 10 mins, this study designed a generalized reduced gradient (GRG) numerical optimization method coupled with PROSAILH_5B radiative transfer model (RTM) to track the sub-daily LFMC dynamics. This method simultaneously accounted for the changing sun-target-sensor geometry bi-directional reflectance distribution function (BRDF) effect on Himawari-8 AHI reflectance. LFMC field measurements from Australia and China validated the LFMC estimation from Himawari-8 AHI. In addition, they were also compared to estimates from two broadly used polar-orbiting satellites, the Landsat-8 OLI and Terra+Aqua MODIS. At the sub-daily scale, the LFMC estimated using the GRG method from Himawari-8 AHI yielded reasonable accuracy (R^2=0.61, rRMSE=20.78%). When averaged to a daily scale, the accuracy of LFMC estimation based on the Himawari-8 AHI was lower (R^2: 0.60-0.61, rRMSE=25.38%-26.58%) than that based on the Landsat-8 OLI (R^2: 0.68-0.79, rRMSE=18.11%-25.89%) and Terra+Aqua MODIS (R^2: 0.63-0.76, rRMSE=19.73%-25.84%). However, after removing some heterogeneous measurements, the difference in the accuracy of LFMC estimates among these three data sources got smaller and improved (R^2: 0.72-0.82, rRMSE=17.96%-23.84%). Furthermore, the method proved its feasibility and applicability to identify fire danger conditions through two wildfire case studies: one in Queensland (Australia, 2019) and another in Xichang (China, 2020). These studies showed that the wildfires started when the Himawari-8 AHI-based sub-daily LFMC reached its daily minimum. Therefore, this study serves as a foundational step toward estimating sub-daily LFMC dynamics, an important yet overlooked factor in assessing sub-daily fire danger and behavior.

Keywords: Wildfires; live fuel moisture content; sub-daily scale; Himawari-8; Geostationary satellite; Numerical optimization; Radiative transfer model

1. Introduction

Wildfires are becoming an increasing threat to many communities worldwide, releasing atmospheric greenhouse gases, accelerating global warming and climate change, and threatening human life and welfare (Argañaraz et al. 2015; Cao et al. 2013; Collins et al. 2021; Johnston et al. 2020; Jolly et al. 2015; Moritz et al. 2012; Nolan et al. 2020; Ward et al. 2020). Near real-time wildfire danger assessment over large areas is thus essential for early warning and management (Chuvieco et al. 2010) and to achieve the 2015 United Nations 2030 Sustainable Development Goals (SDGs). Live fuel moisture content (LFMC), defined as the percentage of water content over dry mass, is a critical variable in fire ignition and spread to understand wildfire risk and its behavior (Gill et al. 1978; Grootemaat et al. 2015; Quan et al. 2023; Quan et al. 2021c; Resco de Dios et al. 2021; Vinodkumar et al. 2021; Yebra et al. 2013). Traditional field sampling for LFMC monitoring shows high accuracy, but is time-consuming, with high costs, and cannot be applied at large scales (Yebra et al. 2019a). Remote sensing techniques can estimate LFMC, providing the opportunity for spatial-temporal continuous monitoring from regional to global scales (Fan et al. 2018; Nolan et al. 2016; Quan et al. 2021c; Rao et al. 2020; Yebra et al. 2013; Zhu et al. 2021).

Previous studies reported LFMC estimates through different satellites, sensors, and reflectance products, such as Sentinel-2A/B (Sibanda et al. 2021), the Landsat series (Garcia et al. 2020; Quan et al. 2017), the Moderate Resolution Imaging Spectroradiometer (MODIS) reflectance products (Arganaraz et al. 2016; Myoung et al. 2018; Yebra et al. 2008; Yebra et al. 2018; Yebra et al. 2019a; Zhu et al. 2021), and the Advanced Very High-Resolution Radiometer (AVHRR) (Garcia et al. 2008). Active and passive microwave remote sensing also produced LFMC estimates (Fan et al. 2018; Jia

et al. 2019; Rao et al. 2020; Tanase et al. 2015; Wang et al. 2019). While promising, these remote sensing technologies can only deliver data at a relatively low temporal resolution (1-16 days), with spatial resolution ranging from 10 m to the tens of km. Among them, MODIS is the most widely used remote sensing data for monitoring LFMC globally, given its moderate spatial resolution (250–1,000 m) and daily temporal resolution with a morning and an afternoon satellite overpass (Yebra et al. 2013).

Despite advances in monitoring LFMC dynamics from daily to seasonal scales, methods to obtain the continuous sub-daily variations (e.g., every 10 mins to hourly during daylight) of LFMC are currently lacking. These sub-daily LFMC variations can be critical, when moving from a wet to a dry season. For example, this transition period lasts only one month in Mediterranean savannas, passing grasslands from fully turgid to completely dry (Luo et al. 2018). Another critical time is during the very high temperatures of the fire-prone season, when vegetation suffers changes in LFMC during the day because their roots are not able to replenish water losses by evapotranspiration. This fact was documented even for irrigated tree plantations from airborne hyperspectral data (Cheng et al. 2013; Cheng et al. 2014). Additionally, the knowledge of sub-daily dynamics of LFMC improves the understanding of wildfire danger variations over the course of a day, enhancing the ability for earlier assessment and control, as well as detection of sub-daily cycling of ecosystem processes (Jeong et al. 2023; Khan et al. 2021; Xiao et al. 2021). To this end, the Advanced Himawari Imager (AHI) onboard the new-generation geostationary meteorological satellite Himawari-8 opens an opportunity for monitoring the sub-daily LFMC dynamics, with observations every 10 mins under Full Disk Mode.

LFMC estimates from remotely sensed spectral data often rely on statistical correlations (Arganaraz et al. 2016; Marino et al. 2020; Nolan et al. 2016). These methods

are easy to implement, but their drawbacks are being sensor and site-specific (Caccamo et al. 2012; Quan et al. 2017; Yebra et al. 2018). In recent years, deep learning models have emerged as a promising data-driven alternative for large-scale LFMC mapping (Miller et al. 2022; Zhu et al. 2021). However, the accuracy of these models is heavily dependent on the availability of ground LFMC samples, thereby limiting their applicability to regions with limited or no ground LFMC measurements. Based on physical laws that consider the mechanistic influence of vegetation on electromagnetic waves, radiative transfer models (RTMs) provide replicable LFMC estimates with explicit connections to canopy spectra (Casas et al. 2014; Marino et al. 2020; Quan et al. 2017; Riaño et al. 2005; Yebra et al. 2018).

The LFMC estimated from RTM requires an appropriate method for model inversion. This typically involves the use of a lookup table (LUT) algorithm (Estevez et al. 2020; Jurdao et al. 2013; Qin et al. 2008; Quan et al. 2021a; Quan et al. 2021c; Yebra et al. 2013). The LUT algorithm is a comprehensive optimization technique that establishes the dimensions of the free variables and step length during the construction of the table. However, the construction of the LUT becomes challenging due to the requirement of multiple input parameters with various directional and spectral configurations (Qin et al. 2008). To use Himawari-8 AHI data, additional computational complexity is needed to account for changes in geometric observation parameters, such as solar zenith and satellite observation angles. To mitigate the LUT algorithm limitations, a numerical optimization-based approach can be employed. This method offers flexibility in dealing with arbitrary directional and spectral configurations, handling numerous variables, and accommodating a wide range of practical scenarios (Fang et al. 2003).

Within this context to improve wildfire planning, prescription, and suppression, this paper assesses the capability of Himawari-8 AHI data to retrieve sub-daily LFMC from RTM inversion through generalized reduced gradient (GRG) numerical optimization-based algorithms with a two-stage inversion strategy. Multiple sources of prior knowledge iteratively constrained the PROSAILH_5B RTM (Feret et al. 2008; Verhoef 1984) to improve the LFMC estimations. Field LFMC measurements from Australia and China validated the Himawari-8 AHI-based LFMC. In addition, results were also compared to Landsat-8 OLI and Terra+Aqua MODIS based LFMC estimates.

2. Data

2.1. LFMC field measurements

LFMC measurements from five Australian and five Chinese sites validated LFMC estimations (Fig. 1 and Table 1). The LFMC from Chinese sites was sampled multiple times during one day between 10:00 AM to 4:00 PM, at 10 mins to 2 hours intervals, including one grassland site in Qinghai Lake Basin (QLB), three evergreen forest sites near the Xichang city (Xichang 1 and Xichang 2) and near the Dali city, and one evergreen forest site in Xisaishan site. The sampling period was selected before or during the fire season for each site. The Australian sites were in the Australian Capital Territory (ACT) and New South Wales (NSW), including one grassland site adjacent to Coppins Crossing Road (ACT, CCR), two evergreen forest sites in Namadgi National Park (NNP1, and NNP2), and two evergreen woodland sites in the Cumberland Plain woodland (Cumberland Plain SuperSite (NSW, CPS) and EucFACE site (NSW, EucFACE)). These Australian sites were sampled once a day between 10:00 AM and 2:00 PM to represent the highest fire danger conditions during the day.

The sample sites were selected to be relatively homogeneous and distributed with the same species. Specifically, the grassland sites (CCR and QLB) in Australia and China consisted of native grass, *Pinus yunnanensis* was predominant at the Xichang site and Dali site, while *bamboo*, *Eucalyptus globulus Labill*, *E. tereticornis*, *E. fibrosa* and *E. moluccana* were at the Xisaishan, the Namadgi, the EucFACE, and the CPS sites, respectively. To match the size of the Himawari-8 AHI pixel, each site had at least 4 km^2, and was commonly larger. Within this size, the species, weather conditions, and terrain were generally consistent across the sites. Despite this, the LFMC validation can also face the additional challenge of the mixed pixel effect on such coarse 2 km Himawari-8 AHI pixels. To assess the homogeneity of the selected sites, the coefficient of variation (CV) was computed using the standard deviation ($NDVI_{SD}$) and mean ($NDVI_{mean}$) of normalized difference vegetation index ($NDVI_{CV}$, Eq. 1 and 2) values from Landsat-8 OLI pixels within each Himawari-8 AHI pixel. The LFMC measurement of a given site served for validation only when the $NDVI_{CV}$ was below 15%, as suggested by Quan et al. (2021c) (Fig. S1).

$$NDVI = \frac{\rho_{NIR} - \rho_{Red}}{\rho_{NIR} + \rho_{Red}} \quad (1)$$

$$NDVI_{CV} = \frac{NDVI_{SD}}{NDVI_{mean}} \times 100\% \quad (2)$$

Samples collected for LFMC and other variables in Chinese sites followed the same protocol, as in previously published studies (Quan et al. 2017; Yebra et al. 2013; Yebra et al. 2019b; Youngentob et al. 2016). The leaf area index (LAI, m^2/m^2) was measured using a fisheye camera system (Hemiview & EOS60D & Sigma EX DC4.5). A laser altimeter (ORPHA 800A) recorded the trees' width, height, shape and crown type. Canopy and understory leaves were sampled to determine the range of chlorophyll a and b content (C_{ab}, $\mu g/cm^2$), leaf area (LA, cm^2), equivalent water thickness (EWT, g/cm^2),

and dry matter content (DMC, g/cm^2). LA was measured in situ using a LI-3000C. A SPAD-502 portable meter measured C_{ab} and converted to μg/cm^2 units based on Eq. (3) (John et al. 1995). The LFMC was collected from both the canopy and understory layers on four sub-sites, including leaves from different branches and trees. Following the method described by Youngentob et al. (2016), leaves from the canopy were collected using an arborist throw-line launcher. The grassland LFMC was collected from all the aboveground live fuel. Placed in a sealed bag, the collected samples returned to the laboratory for weighing (W_{fresh}) and then they were transferred to paper bags to be oven-dried for 24 h at 105 °C (Matthews 2010). Once dried, the samples were weighed again to determine the dry weight (W_{dry}). The LFMC, EWT and DMC of each sample were calculated as the percentage difference of fresh and dry weight (Eq. 4-6). The mean LFMC value from these samples was calculated to represent the LFMC at that particular site. This approach minimized the effects of individual leaf variation and ensured that the sample size was sufficient for comparison across different times and seasons. The LFMC measurements for Australian sites were available from previously published works in Griebel et al. (2023); Nolan et al. (2022); and Yebra et al. (2018) (Table 1).

$$C_{\text{ab}} = 10^{SPAD^{0.265}} \times 0.08955,\ SPAD \in (1,100) \quad (3)$$

$$LFMC = \frac{W_{fresh} - W_{dry}}{W_{dry}} \times 100\% \quad (4)$$

$$EWT = \frac{W_{fresh} - W_{dry}}{LA} \quad (5)$$

$$DMC = \frac{W_{dry}}{LA} \quad (6)$$

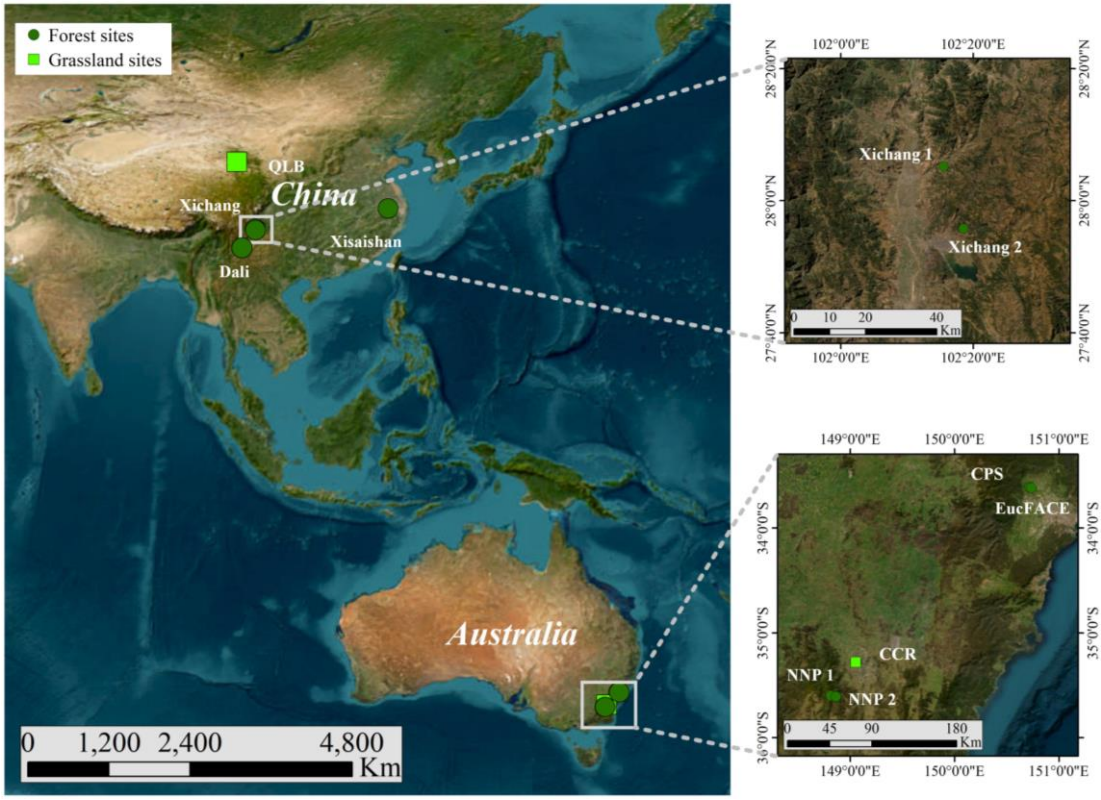

Fig. 1 Validation sites in Australia and China with background map from the World Imagery (Environmental Systems Research Institute, ESRI, https://services.arcgisonline.com/arcgis/rest/services/World_Imagery/MapServer). Acronyms are explained in Table 1.

Table 1. LFMC measurements in China and Australia.

Country	Sites	Fuel class	Sampling time	Latitude	Longitude	Count	Sources
Australia	Coppins Crossing Road (CCR)	Grassland	October 1, 2015 - April 20, 2016	−35.2787	149.0559	33	Yebra et al. (2018)
	Namadgi National Park 1 (NNP1)	Forest	October 1, 2015 - April 20, 2016	−35.5979	148.8165	19	Yebra et al. (2018)
	Namadgi National Park 2 (NNP2)	Forest	October 1, 2015 - April 20, 2016	−35.6071	148.8657	18	Yebra et al. (2018)
	Cumberland Plain SuperSite (CPS)	Woodland	December 3, 2018 - September 4, 2019	−33.61	150.72	9	Nolan et al. (2022)
	EucFACE	Woodland	August 23, 2018 – June 18, 2021	−33.619	150.738	13	Griebel et al. (2023)
China	Qinghai Lake Basin (QLB)	Grassland	July 28 - August 2, 2015	99.5861	37.2040	70	This study
	Xichang 1	Forest	December 6-9, 2020	28.2569	102.2915	12	This study
	Xichang 2	Forest	March 16-20, 2021	27.9277	102.2941	23	This study

Xisaishan	Forest	January 6-8, 2023	30.7801	119.9984	9	This study
Dali	Forest	March 20-25, 2023	25.9942	100.3166	54	This study

2.2. *Satellite data*

2.2.1 Himawari-8 AHI data

The Japan Meteorological Agency (JMA, https://www.eorc.jaxa.jp/ptree/) issues the standard Himawari-8 AHI albedo product (Level 1 Gridded full disk). The product is generated from the Himawari Standard Data, re-sampled to equal latitude-longitude grids, with 500m–2km spatial resolution and 10 mins temporal resolution. For each site in Australia and China (Table 1), this study downloaded the corresponding Himawari-8 AHI images between 9:00 AM and 5:00 PM (GMT+8 for China/GMT+10 for Australia) at 10-mins intervals with 2km spatial resolution. Furthermore, Himawari-8 AHI images were geometrically corrected at nadir and atmospherically corrected with the Simplified and Robust Surface Reflectance Estimation Method (SREM) method (Bilal et al. 2019). The SREM was constructed based on the satellite signal in the solar spectrum radiative transfer model equations, without integrating information on aerosol particles and atmospheric gases.

To select clear sky pixels, this study utilized the atmospheric parameter products, e.g., Aerosol Optical Thickness, Cloud Optical Thickness, and Cloud Type, obtained from the JAXA Himawari Monitor P-Tree System (Ishimoto et al. 2012, 2013; Letu et al. 2016; Letu et al. 2014; Letu et al. 2019; Letu et al. 2012; Masuda et al. 2012; Nakajima et al. 2011). These products are available every 10 mins at 5 km scale for full-disk. Analysis of all these products and their cross-validation ensured the accuracy. The sky conditions based on the weather conditions observed during fieldwork designated pixels depicting clear skies. Finally, the Cloud Optical Thickness product was selected to

identify the weather conditions corresponding to the fieldwork records. By considering this product and the $NDVI_{CV}$ < 15% (Eq. 2), 18 grassland measurements and 7 forest LFMC measurements were excluded from the assessment of satellite-derived LFMC estimates.

2.2.2 Landsat-8 OLI

Landsat-8 OLI standard reflectance product was downloaded from the United States Geological Survey (USGS, https://earthexplorer.usgs.gov). This product includes seven bands spanning from visible (VIS) to shortwave infrared (SWIR), with a spatial resolution of 30 m, and is updated every 16 days. This analysis retained only the matches between field measurements and the closest available time for a Landsat-8 image. Additionally, a quality assurance (QA) value of 322 in the Landsat-8 OLI QA product selected cloud-free observations.

2.2.3 Terra+Aqua MODIS

The Nadir Bidirectional Reflectance Distribution Function Adjusted Reflectance (MCD43A4.006) (Schaaf et al. 2002), the Fraction of Photosynthetically Active Radiation (FPAR) and LAI (MCD15A3H.006) (Myneni et al. 2002) MODIS products were downloaded from the Land Processes Distributed Active Archive Center (LPDAAC) at the USGS Earth Resources Observation and Science Center (EROS) (http://lpdaac.usgs.gov). The selection of the Quality Assessment flag with ideal quality (QA=0) of the closest time at each location within 16 days ensured the excellence of the 500 m MCD43A4.006 reflectance data. The MCD15A3H.006 consists of a 4-day LAI composite at 500 m. Only 'good quality' pixels without cloud, snow, and shadow according to the "FparLai_QC" and "FparExtra_QC" layers provided the initial LAI value to estimate LFMC in the numerical optimization process (Section 3.5).

3. Methods

Prior information from field measurements and literature review parameterized the PROSAILH_5B RTM with ecological rules to constrain the RTM inversion. The numerical optimization method of GRG optimized the RTM for robust and accurate LFMC estimation from Himawairi-8 AHI, Landsat-8 OLI, and MCD43A4 products. Furthermore, the free variables in the PROSAILH_5B RTM have different spectral sensitivities. To address this issue, a two-stage inversion strategy optimized the sensitive variables first and then the least-sensitive variables. Finally, the field LFMC campaigns conducted once a day in Australia and sub-daily in China validated the LFMC estimates from Himawari-8 AHI, and served for comparison between the performance of LFMC estimates from the three above mentioned remote sensing products.

3.1 PROSAILH_5B parameterization

The PROSAILH_5B RTM estimated LFMC from Himawari-8 AHI data. The performance of this RTM to estimate LFMC has been widely verified and applied in previous studies (Quan et al. 2015; Quan et al. 2017; Riaño et al. 2005; Yebra and Chuvieco 2009; Yebra et al. 2018). It takes the output of leaf reflectance and transmittance of the PROSPECT leaf optical model (Feret et al. 2008; Jacquemoud and Baret 1990) into the canopy bidirectional reflectance SAILH model (Scattering by Arbitrary Inclined Leaves with a hot spot) (Kuusk 1991; Verhoef 1984).

PROSPECT leaf optical model is widely applied for broad leaves and it is still reasonable for needle leaves (Cheng et al. 2006). PROSPECT-5 requires leaf variables, such as leaf structure parameter (N, unit-less), DMC (g/cm^2), EWT (g/cm^2), and main pigment contents, i.e., C_{ab} ($\mu g/cm^2$), leaf brown pigment content (C_{bp}, unit-less) and

carotenoid content (C_{ar}, μg/cm^2). To simulate the canopy spectra, SAILH also requires LAI, hot spot factor (hspot, unit-less), two leaf inclination distribution function parameters ($LIDF_a$ and $LIDF_b$), sun zenith angle (tts, °), observer zenith angle (tto, °), relative azimuth angle (psi, °) and a soil factor (psoil, unit-less) ranging from 0 (wet soil) to 1 (dry soil) to characterize the soil moisture level.

Based on the field measurements and previous studies (Casas et al. 2014; Quan et al. 2015; Quan et al. 2017; Yebra et al. 2008), the input values in Table 2 parameterized PROSAILH_5B RTM. The least sensitive parameters, i.e., N, C_{bp}, C_{ar}, and hspot were set to the empirical values for grassland and forest regions (N=2, C_{bp}=0, C_{ar}=8 μg/cm^2, hspot=0.01). LIDF was set to erectophile, spherical, and planophile for grasslands (Wang et al. 2013) and ellipsoidal for forests (Casas et al. 2014). Following previous PROSAILH studies (Bowyer and Danson 2004; Casas et al. 2014; Quan et al. 2021c; Riaño et al. 2005; Yebra and Chuvieco 2009; Yebra et al. 2008), LFMC estimation was sensitive to the vegetation and soil variables of C_{ab}, EWT, DMC, LAI, and psoil. Therefore, they were set as free variables. The geometric parameters (i.e., tto, tts, psi) are available in each satellite metadata and vary according to the sampling date, region, latitude, and sensor type, challenging the model parameterization in Table 2.

Table 2. PROSAILH_5B parameterization for Himawari-8 AHI based LFMC estimations in Australia and China.

RTMs	Input parameters	Variable	Unit	China	Australia
PROSPECT-5	Leaf structure parameter	N	/	2	2
	Chlorophyll *a* + *b* content	C_{ab}	μg/cm^2	20-60	20-60
	Equivalent water thickness	EWT	g/cm^2	0.001-0.03 (Grassland); 0.004-0.02 (Forest)	0.001-0.017 (Grassland); 0.001-0.03 (Forest/Woodland)
	Dry matter content	DMC	g/cm^2	0.005-0.015 (Grassland); 0.001-0.015 (Forest)	0.005-0.015 (Grassland); 0.001-0.015 (Forest/Woodland)
	Brown pigment	C_{bp}	/	0	0
	Carotenoid content	C_{ar}	μg/cm^2	8	8
SAILH-4	Sun zenith angle	tts	°	30-50	14-55
	View zenith angle	tto	°	30-60	30-50
	Relative azimuth angle	psi	°	0-130	2-64
	Leaf area index	LAI	m^2/m^2	0.1-7.0 (Grassland); 0.5-3.0 (Forest)	0.3-3.5 (Grassland); 0.3-5.0 (Forest/Woodland)
	Hot spot factor	hspot	/	0.01	0.01
	Two leaf inclination distribution function (LIDF) parameters	LIDFa LIDFb	/	Grassland (erectophile, spherical, and planophile); Forest (ellipsoidal)	Grassland (erectophile, spherical, and planophile); Forest/Woodland (ellipsoidal)
	Soil factor	psoil	/	0.2-1.0 (Grassland); 0.3-1.0 (Forest)	0.3-1.0 (Grassland); 0.2-1.0 (Forest/Woodland)

3.2 Ecological rules

A major challenge for RTM-based LFMC estimations is the broadly known ill-posed inversion problem, in which different RTM input combinations correspond to almost identical spectra (Quan et al. 2015; Yebra and Chuvieco 2009; Yebra et al. 2013). Consequently, it confuses the inversion to retrieve LFMC accurately. Yebra and Chuvieco (2009) pointed out that the RTM input variables are not independent of each other, but they are naturally correlated. Ignoring this fact generates unrealistic spectra that aggravate this ill-posed inversion problem.

To address this issue, ecological rules regularize the RTMs to make the LFMC simulation scenario more realistic (Quan et al. 2021c; Yebra et al. 2008). Here, the ecological rules among LFMC, LAI, and EWT were mainly derived from the field measurements taken in this study and also from the measurements in LOPEX1993 (Hosgood et al. 1995) and ANGERS2003 (Feret et al. 2008) leaf optical properties databases (Fig. 2). This prior information is explained in detail in Quan et al. (2021b). According to field measurements, Chinese sites exhibited an overall clear positive linear relationship between LFMC and LAI (R^2=0.37, p<0.05) or EWT (R^2=0.18, p<0.05) for grasslands, as well as LAI for forest (R^2=0.43, p<0.05). In Australia, there was a strong correlation between grassland LFMC and LAI estimates form MCD15A3H.006 (R^2=0.90, p<0.05), whereas forest LFMC showed a weaker correlation with LAI (R^2=0.29, p<0.05). Following Quan et al. (2021c), the RTM modelling phase introduced these relationships by adopting Eq. (7) to calculate the joint posterior probability distribution of the more likely variable combinations:

$$f(x,y) = \left(1 - \frac{g(x,y)}{MAX(|g(x,y)|)}\right)^{r \times k} \quad (7)$$

where x and y are the variables between LAI, LFMC, and EWT; the $f(x,y)$ is the joint posterior probability distribution of x and y variables; $g(x,y)$ is the fitted function in Fig. 2; r is the correlation coefficient and k is a controlling factor that a higher k value can generate more constrained variable combinations (k = 10, following Quan et al., 2021b). This approach removed unrealistic simulation scenarios.

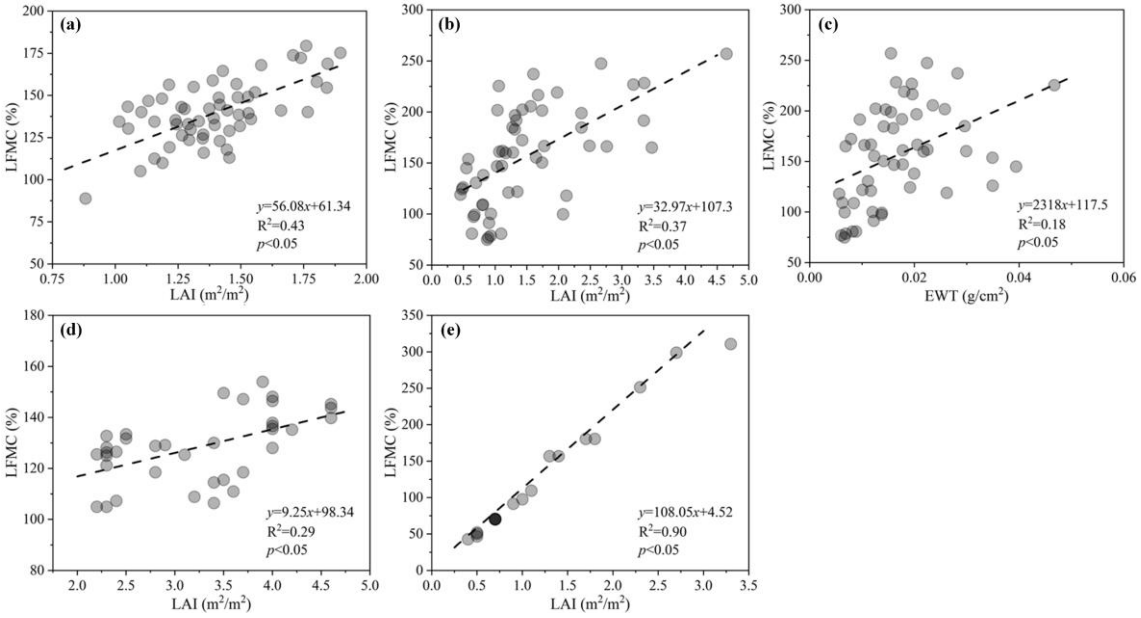

Fig. 2 Scatterplots of the relationships between LFMC and LAI or EWT for forest (a) and grasslands (b-c) in China; and forests (d) and grasslands (e) in Australia. Only the relationships with p<0.05 were shown here and selected as ecological rules to constrain the RTM inversion.

3.3 The numerical optimization GRG method

The RTM-LUT inversion is broadly preferred as an optimization method in the literature (Casas et al. 2014; Jurdao et al. 2012; Quan et al. 2021c; Yebra et al. 2018). Nevertheless, it is not computationally feasible to apply it for the Himawari-8 AHI-based LFMC estimation here. The changing sun-target-sensor geometry every 10 minutes would make the LUT dimension extremely high to account for the BRDF effect properly.

The built LUT would also be infeasible when applied to other regions with different circumstances than China and Australia, since the changing rates in tto, tts, and psi vary from region to region. Additionally, arbitrary prior linear or non-linear information cannot be updated into the inversion process without rebuilding the LUT. To overcome this situation, this study applied a GRG to optimize the RTM. Arbitrary directional and spectral configurations with numerous variables and prior information can easily extend this method. GRG solves the optimization problem with the gradient and feasible direction of the target function. This method requires a cost function determination between the simulated and observed spectrum. To build this cost function (*T*, Eq. 8), this study selected the most broadly used Vegetation indices (VIs) that are sensitive to vegetation moisture variation (Caccamo et al. 2012; Nolan et al. 2016; Quan et al. 2017; Quan et al. 2021c; Yebra and Chuvieco 2009; Yebra et al. 2018): NDVI (Eq. 1), enhanced vegetation index (EVI, Eq. 9), normalized difference infrared index (NDII, Eq. 10) and visible atmospheric resistant index (VARI, Eq. 11).

$$T = \sqrt{\sum(VI_{observation} - VI_{simulation})^2}, VI \in (NDVI, EVI, NDII\ and\ VARI) \quad (8)$$

$$EVI = 2.5 \times \frac{\rho_{NIR} - \rho_{Red}}{\rho_{NIR} + 6 \times \rho_{Red} - 7.5 \times \rho_{Blue} + 1} \quad (9)$$

$$NDII = \frac{\rho_{NIR} - \rho_{SWIR}}{\rho_{NIR} + \rho_{SWIR}} \quad (10)$$

$$VARI = \frac{(\rho_{Green} - \rho_{Red})}{(\rho_{Green} + \rho_{Red} - \rho_{Blue})} \quad (11)$$

where $VI_{observation}$ and $VI_{simulation}$ are the four observed VIs from satellite observations and simulated VIs from PROSAILH_5B RTM, respectively. The ρ_{NIR}, ρ_{Red}, ρ_{Green}, $\rho_{Blue,}$ and ρ_{SWIR} are the NIR, Red, Green, Blue, and SWIR reflectance bands, respectively. Furthermore, the spectral response functions for each band of the Himawari-8 AHI convolved the simulated spectra and VI to match the actual Himawari-8 AHI data.

Traditionally, the LFMC estimation is a constrained optimization problem and can be described in Eq. (8). The cost function *T* can be expressed as a composite function of five free variables, i.e., C_{ab}, EWT, DMC, LAI, and psoil (Eq. 12 and 13). For simplicity, the variable LFMC substituted the variable DMC in the inversion procedure (LFMC=EWT/DMC×100%) (Yebra et al. 2013). The optimal solution is the set of input variables corresponding to the minimum *T* value (min $\boldsymbol{T}$ (X)).

$$\min T(\mathbf{X}) \quad \boldsymbol{l} \le \mathbf{X} \le \boldsymbol{u}$$

$$\mathbf{X} = \begin{bmatrix} C_{ab} \\ EWT \\ LFMC \\ LAI \\ psoil \end{bmatrix} \boldsymbol{l} = \begin{bmatrix} l_{C_{ab}} \\ l_{EWT} \\ l_{LFMC} \\ l_{LAI} \\ l_{psoil} \end{bmatrix} \boldsymbol{u} = \begin{bmatrix} u_{C_{ab}} \\ u_{EWT} \\ u_{LFMC} \\ u_{LAI} \\ u_{psoil} \end{bmatrix} \tag{12}$$

$$VI_{simulation} = PROSAILH(Cab, EWT, LFMC, LAI, psoil) \tag{13}$$

where X is the vector of independent free variables in PROSAILH_5B RTM, i.e., **X**= (C_{ab}, EWT, LFMC, LAI, psoil), with an upper boundary ($\boldsymbol{u}$) and lower boundary ($\boldsymbol{l}$). The PROSAILH_5B parameterizations determine the initial boundaries (Table 2).

The partial derivative of each variable (the *i*th component of $\boldsymbol{X}$, i.e., x_i) in the function follows the chain rule shown in Eq. (14). However, the direct calculation of the partial derivative of each variable is highly complicated, since the cost function *T* contains the complex PROSAILH_5B function. Hence, the TAPENADE toolkit (version: 3.6, https://team.inria.fr/ecuador/en/tapenade), an Automatic Differentiation Engine developed by the Tropics and Ecuador teams, solved the gradient (∇T) to search for the optimal solution. This toolkit obtains the partial *T* derivative to each variable (x_i) establishing the adjoint PROSAILH_5B model (Qin et al. 2008), which is defined as the partial derivative of this model to each variable (x_i), i.e., $\frac{\partial \rho(\boldsymbol{X})}{\partial x_i}$.

$$\begin{cases} \nabla T = \left(\frac{\partial T}{\partial C_{ab}}, \frac{\partial T}{\partial EWT}, \frac{\partial T}{\partial LFMC}, \frac{\partial T}{\partial LAI}, \frac{\partial T}{\partial psoil}\right) \\ \frac{\partial T}{\partial x_i} = \left(\frac{\partial T}{\partial y}\Big|_{y=\rho(\boldsymbol{X})}\right)\frac{\partial \rho(\boldsymbol{X})}{\partial x_i}, \rho(\boldsymbol{X}) = PROSAILH(\boldsymbol{X}) \end{cases} \quad (14)$$

To solve constrained numerical optimization problems, the GRG first calculates the feasible direction gradient ($\boldsymbol{d}_k$), considering the boundary conditions of the variables using Eq. (15).

$$\begin{aligned} r_i^k &= -\frac{\partial T}{\partial x}\Big|_{x=x_i^k} \\ d_i^k &= \begin{cases} 0, \ (x_i^k = l_i^k, r_i^k > 0) \parallel (x_i^k = u_i^k, r_i^k < 0) \\ r_i^k, \ (l_i^k < x_i^k < u_i^k) \parallel (x_i^k = l_i^k, r_i^k < 0) \parallel (x_i^k = u_i^k, r_i^k > 0) \end{cases} \\ \boldsymbol{X}_k &= \begin{bmatrix} C_{ab}^k \\ EWT^k \\ LFMC^k \\ LAI^k \\ psoil^k \end{bmatrix} \quad \boldsymbol{l}_k = \begin{bmatrix} l_{C_{ab}}^k \\ l_{EWT}^k \\ l_{LFMC}^k \\ l_{LAI}^k \\ l_{psoil}^k \end{bmatrix} \quad \boldsymbol{u}_k = \begin{bmatrix} u_{C_{ab}}^k \\ u_{EWT}^k \\ u_{LFMC}^k \\ u_{LAI}^k \\ u_{psoil}^k \end{bmatrix} \quad \boldsymbol{d}_k = \begin{bmatrix} d_{C_{ab}}^k \\ d_{EWT}^k \\ d_{LFMC}^k \\ d_{LAI}^k \\ d_{psoil}^k \end{bmatrix} \end{aligned} \quad (15)$$

where l_i^k is the lower bound ($\boldsymbol{l}_k$) of x_i in the kth iteration and u_i^k is its upper bound ($\boldsymbol{u}_k$). The PROSAILH_5B model parameterizations and constraints described in Eq. (8) determine the x_i bound (see Section 3.1). The rule in Eq. (16) determines the search step length (λ_k), where λ_0 is the maximal step.

$$\lambda_k = \max\{\lambda \mid \boldsymbol{l}_k \leqslant \begin{bmatrix} C_{ab}^k + \lambda d_{C_{ab}}^k \\ EWT^k + \lambda d_{EWT}^k \\ LFMC^k + \lambda d_{LFMC}^k \\ LAI^k + \lambda d_{LAI}^k \\ psoil^k + \lambda d_{psoil}^k \end{bmatrix} \leqslant \boldsymbol{u}_k \ , \lambda = \lambda_0, \frac{1}{2}\lambda_0, \frac{1}{4}\lambda_0, \ldots\} \quad (16)$$

If λ_k is found, Eq. 17 updates $\boldsymbol{X}$ and then $\boldsymbol{l}_k$ and $\boldsymbol{u}_k$, according to the constraints in Fig. 2 and Eq. (7).

$$\boldsymbol{X}_{k+1} = \begin{bmatrix} C_{ab}^{k+1} \\ EWT^{k+1} \\ LFMC^{k+1} \\ LAI^{k+1} \\ psoil^{k+1} \end{bmatrix} = \begin{bmatrix} C_{ab}^k + \lambda_k d_{C_{ab}}^k \\ EWT^k + \lambda_k d_{EWT}^k \\ LFMC^k + \lambda_k d_{LFMC}^k \\ LAI^k + \lambda_k d_{LAI}^k \\ psoil^k + \lambda_k d_{psoil}^k \end{bmatrix} \quad (17)$$

Finally, when Eq. (18) meets the condition, the iteration stops and exports $\boldsymbol{X}_{k+1}$.

$$|\boldsymbol{d}_{k+1}| = \sqrt{(d_{C_{ab}}^{k+1})^2 + (d_{EWT}^{k+1})^2 + (d_{LFMC}^{k+1})^2 + (d_{LAI}^{k+1})^2 + (d_{psoil}^{k+1})^2} \leq \varepsilon \quad (18)$$

where $\boldsymbol{d}_{k+1}$ is the feasible direction gradient in the k+1th iteration and ε is the margin of deviation.

3.4 Two-stage inversion strategy

As shown in Table 3, the five free variables have different sensitivities to the canopy spectra. EWT, LAI, and psoil are sensitive to the canopy spectra with the high absolute partial derivative of T (i.e., $|\frac{\partial T}{\partial x}|$ in Table 3), whereas LFMC and C_{ab}, are weakly sensitive to the simulated canopy reflectance with much slighter gradients (i.e., 10^{-4} - 10^{-3}). If deriving all five parameters simultaneously, slow convergence speed and small search step length occur. To solve this issue, a two-stage inversion strategy estimates firstly the sensitive parameters (LAI, EWT, and psoil as X) and secondly the weak ones (LFMC and DMC as X') (Fig. 3). T_1 is the function of the sensitive parameters in the first stage, in which the updated LFMC and C_{ab} are input as constants. Meanwhile, T_2 is the LFMC and C_{ab} function in the second stage, with EWT, LAI, and psoil updated in the first stage as constants. To match the different sensitivity of these five variables, the deviation margins (ε_1 and ε_2) are also set to be different. The initialization parameters (λ_0 and ε) are determined at the beginning of the LFMC inversion procedure, since they affect the convergence speed and accuracy of the estimation. The smaller λ_0 and ε give rise to slower convergence with higher accuracy. In the numerical iteration process, the original range of each free variable (Table 3) and ecological rules (Fig. 2) constrain the upper and lower boundaries of each free variable to alleviate the ill-posed inversion problem by:

$$\boldsymbol{l}_k = \begin{bmatrix} l^k_{C_{ab}} \\ \max(l^k_{EWT}, EWT_{LFMC^k} - RMSE_{EWT\text{-}LFMC}) \\ \max(l^k_{LFMC}, LFMC_{LAI^k} - RMSE_{LFMC\text{-}LAI}) \\ \max(l^k_{LAI}, LAI_{LFMC^k} - RMSE_{LAI\text{-}LFMC}) \\ l^k_{psoil} \end{bmatrix} \le \boldsymbol{X}_k = \begin{bmatrix} C^k_{ab} \\ EWT^k \\ LFMC^k \\ LAI^k \\ psoil^k \end{bmatrix} \le \boldsymbol{u}_k = \begin{bmatrix} u^k_{C_{ab}} \\ \min(u^k_{EWT}, EWT_{LFMC^k} + RMSE_{EWT\text{-}LFMC}) \\ \min(u^k_{LFMC}, LFMC_{LAI^k} + RMSE_{LFMC\text{-}LAI}) \\ \min(u^k_{LAI}, LAI_{LFMC^k} + RMSE_{LAI\text{-}LFMC}) \\ u^k_{psoil} \end{bmatrix} \quad (19)$$

where $\boldsymbol{l}_k$ is the lower bound of X_k in the kth iteration and $\boldsymbol{u}_k$ is the upper bound.

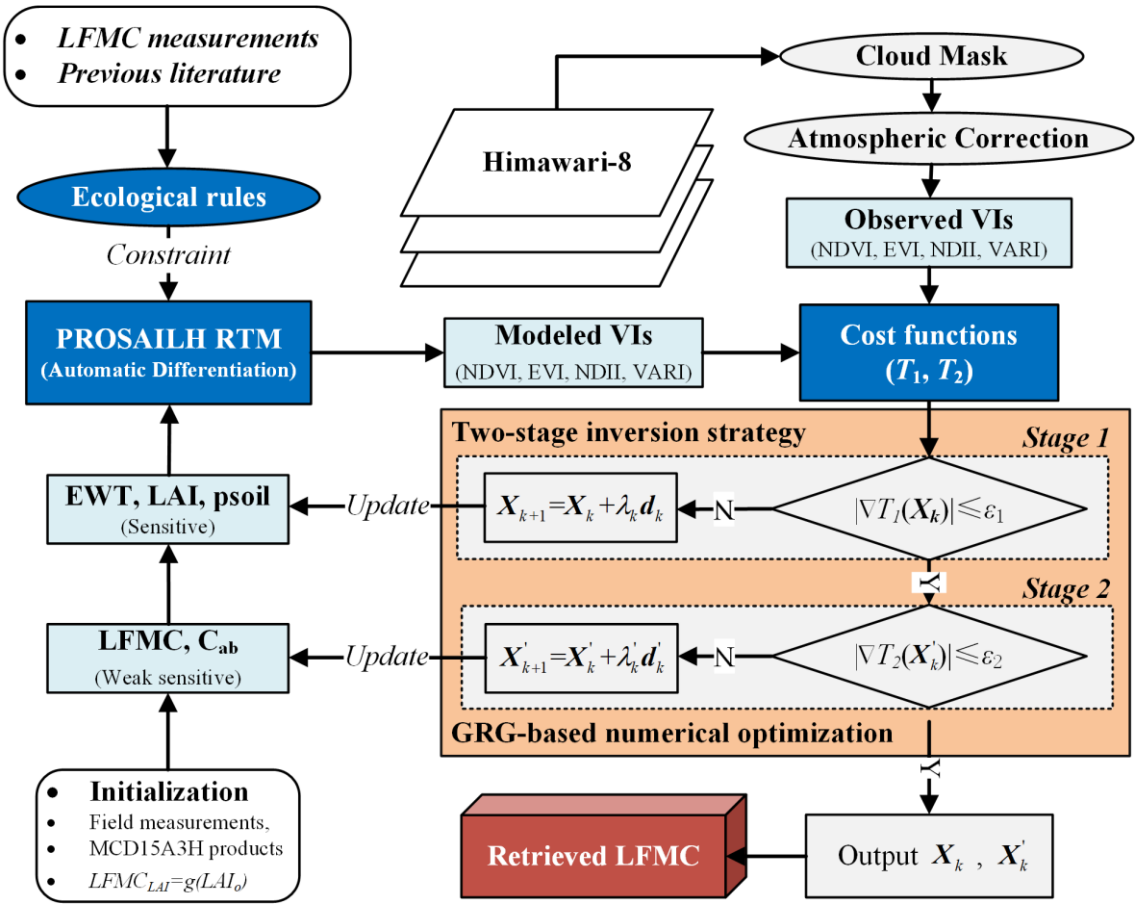

Fig. 3 Methodological flowchart for the two-stage inversion strategy.

Due to the higher gradient of EWT, LAI, and psoil than LFMC and C_{ab}, these three free variables can fall into a local optimum. To solve this problem, a step search strategy creates a grid with the initial parameters (i.e., EWT, LAI, and psoil) in terms of their ranges and mean values (Table 3) in the first stage. This procedure reaches the final

optimization by integrating the objective function values and the corresponding derivative values.

Table 3. Sensitivity and initialization of free variables at the two stages

Stage	Variables	$\lvert\frac{\partial T}{\partial x}\rvert$ ranges
Stage1	EWT	0.1 - 10
	LAI	0.1 - 2
	psoil	0.1 - 2
Stage2	LFMC	10^{-4} - 10^{-3}
	C_{ab}	

3.5 Initialization parameters of the GRG-PROSAILH_5B

For robust, accurate, and effective LFMC estimation, Table 4 summarizes the suitable combination of the initialization of five free parameters, λ_0, and ε. The average field measurements of 0.017 g/cm^2 for grasslands and 0.01 g/cm^2 for forests in the Chinese sites and 0.01 g/cm^2 in the Australian sites set the initial EWT, based on the field measurements and leaf optical properties databases (Fig. 2). The MCD15A3H LAI product set the initial LAI, averaged within a Himawari-8 AHI pixel scale, for the corresponding sampling time and sites in China and Australia. The psoil initial was 0.5, representing a moderate soil moisture condition. The empirical equation between LFMC and LAI (from the MCD15A3H product) rendered the initial LFMC (Fig. 2), while the average value of the feasible range provided the initial C_{ab} to 40 μg/cm^2.

In the first stage of the LFMC inversion procedure, λ_0 was 1 for grasslands and forests with a narrow feasible range of 1-10. The ε_1 settings were 0.1 for grasslands and 4 for forests since there was a larger *T* gradient to the sensitive parameters (EWT, LAI, and psoil). In the second stage, the maximum step length (λ'_0) was limited to the wide feasible range (500-5000), due to the smaller *T* gradient to weakly sensitive parameters, LFMC and C_{ab}. Here, the λ'_0 for grasslands and forests were fixed to 2000 and 1000,

respectively. The deviation margin (ε_2) has a much narrower range of 10^{-6}-10^{-5} and it was fixed as 10^{-6}, to ensure the LFMC estimations accuracy.

Table 4. Range and initialization parameters values for LFMC estimations.

Stage	Parameters	Ranges		Initial values	
		Grassland	Forest	Grassland	Forest
stage1	λ_0	1-10		1	
	ε_1	0.1-1	1-5	0.1	4
	EWT	/		0.017g/cm^2 (China) 0.01g/cm^2 (Australia)	0.01g/cm^2 (China) 0.01g/cm^2 (Australia)
	LAI			MCD15A3H/measured LAI	
	psoil			0.5	
stage2	λ_0'	500-5000		2000	1000
	ε_2	10^{-6}-10^{-5}		10^{-6}	
	LFMC	/		$LFMC_{LAI} = g(LAI_0)$, in Fig. 2	
	C_{ab}			40μg/cm^2	

3.6 Assessing LFMC estimations

3.6.1 Validation with in-situ measurements

The *in-situ* LFMC measurements from ten sites in Australia and China in Table 1 and Fig. 1 validated the sub-daily LFMC estimation from the Himawari-8 AHI data. The LFMC measurements obtained from the Chinese sites were taken at the sub-daily scale to validate the LFMC estimation derived from the closest time in the Himawari-8 AHI data. Conversely, the LFMC measurements acquired from the Australian sites were collected on a daily scale, specifically between 10:00 AM and 2:00 PM. Therefore, the LFMC was initially estimated during this time and subsequently averaged to be compared with the daily sampled LFMC measurements. The GPS was used to determine the location of the sampling plots to match the Himawari-8 AHI pixel. As detailed in section 2.1, each site was homogeneous at the pixel size to ensure that the LFMC measurements aligned with the Himawari-8 AHI observation. Subsequently, the corresponding optimal Himawari-8 AHI pixel was chosen to be positioned within each site, while making efforts to avoid mixing it with bare soil, water bodies, buildings, and other non-vegetation obstructions.

Two metrics characterized the LFMC estimates accuracy level, R^2 (Eq. 20) and relative RMSE (rRMSE, Eq. 21 and 22).

$$R^2 = 1 - \frac{\sum_{k=1}^{m}(M_k - E_k)^2}{\sum_{k=1}^{m}(M_k - \overline{M_k})^2} \quad (20)$$

$$RMSE = \sqrt{\frac{\sum_{k=1}^{m}(M_k - E_k)^2}{m}} \quad (21)$$

$$rRMSE = \frac{RMSE}{\overline{M_m}} \quad (22)$$

where M_k and E_k are the k^{th} measured and estimated LFMC, $\overline{M_m}$ is the mean value of LFMC measurements and m is the number of observations. The rRMSE is calculated as RMSE divided by the mean of the variable measured in the field. The rRMSE allows the comparison between variables of different ranges, since it is insensitive to the magnitude of values and less sensitive to outliers (Casas et al. 2014; Richter et al. 2012).

3.6.2 LFMC estimates from Landsat-8 OLI and MCD43A4 at daily scale

This study also compared the daily scale LFMC estimations between Himawari-8 AHI and those taken at the same time once a day from broadly used polar-orbiting Landsat-8 OLI and MODIS satellites. The averaged LFMC estimated from the Himawari-8 AHI data between 10:00 AM and 10:40 AM was compared to the Landsat-8 OLI data, since the Landsat-8 OLI overpasses these sites around that time. Likewise, the average LFMC estimated from the Himawari-8 AHI data between 10:30 AM and 1:30 PM was compared to that from MCD43A4 MODIS product that combines data from MODIS Terra ~10:30 AM and MODIS Aqua ~1:30 PM overpasses.

To assess the potential impact of varying spatial resolution from different image sources on LFMC estimates, this study estimated LFMC from Landsat-8 OLI and MCD43A4 in two ways: using their original spatial resolution of 30 m for Landsat-8 OLI and 500 m for the MCD43A4, as well as resampling them to 2 km to match the resolution of AHI data. To evaluate the effect of homogeneity on LFMC estimate, two possible

thresholds of <15% or <10% $NDVI_{CV}$ from Landsat-8 OLI restricted the LFMC measurements for validation. The LFMC estimation process was consistent across all three satellite datasets, except for tts, tto, and psi parameters for the Landsat-8 and MCD43A4 (Table 5), which were sourced from the metadata of each respective satellite image.

Table 5. Parameterization of tts, tto, and psi in PROSAILH_5B for LFMC estimation from the Landsat-8 OLI and Terra+Aqua MODIS data.

Parameters	Unit	China		Australia	
		Landsat-8	MODIS	Landsat-8	MODIS
tts	°	30-50	30-55	14-48	14-48
tto	°	0	10	0	10
psi	°	0	0	0	0

3.6.3 LFMC application to the Queensland and Xichang wildfire cases

This study further examined whether the Himawari-8 AHI can track the sub-daily changes in LFMC before the occurrence of wildfires. For this purpose, the Xichang wildfire in southwest China and the Queensland wildfire in southeast Australia were analysed (Fig. 4). The Xichang wildfire, which occurred on March 30th, 2020, affected an area of 3,047 ha and mainly comprised evergreen forests. It is the latest severe wildfire event in China, resulting in the unfortunate lost of 19 firefighters during suppression efforts. Meanwhile, the Australia 2019/2020 fires led to extensive forest destruction in southeastern Australia, as documented in previous studies (Bowman et al. 2020; Collins et al. 2021; Nolan et al. 2020). The selected case study for the Queensland wildfire started on September 4th, 2019, and encompassed an area of 10,000 ha. This site consisted of open shrublands, a mixture of woody savannas, and evergreen broadleaf forests, as determined by the MODIS land cover product MCD12Q1 Collection 6.

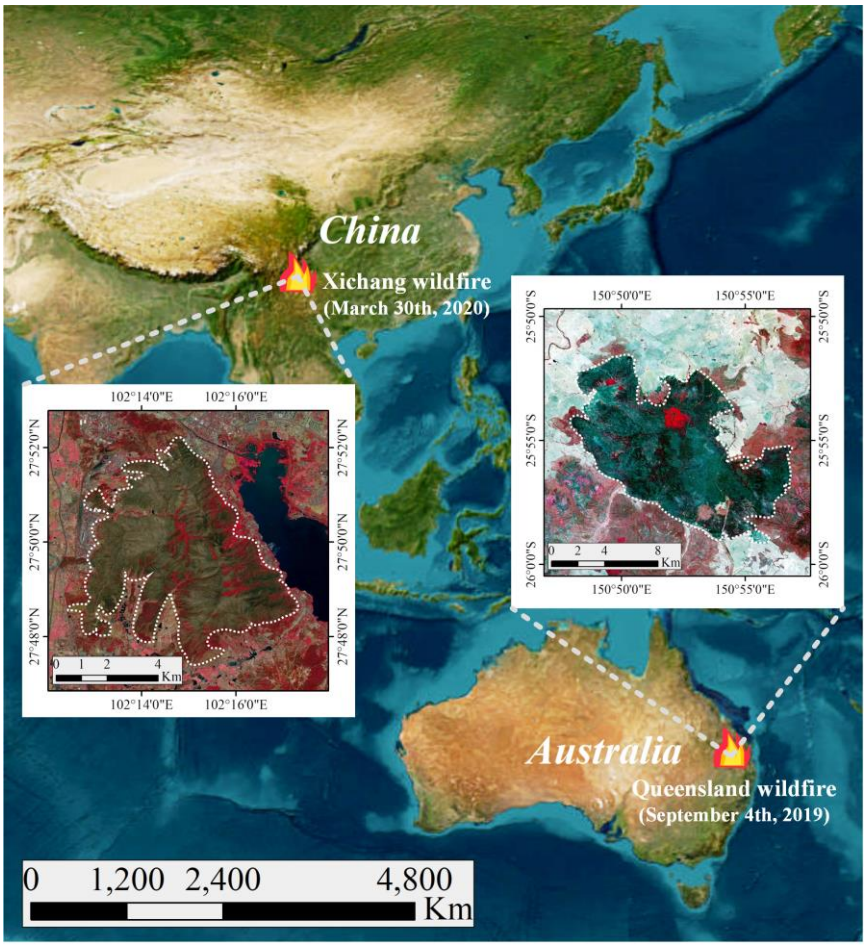

Fig. 4 Wildfire locations in Xichang and Queensland, depicted alongside a false colour composite from Sentinel-2 Multispectral Instrument (MSI) captured on May 4th, 2020, for the Xichang wildfire and September 15th, 2019, for the Queensland wildfire. The composite showcases the NIR, Red, and Blue channels, highlighting burned areas in dark tones due to their distinct spectral signatures

4. Results

4.1 Validation of Himawari-8 AHI estimates with in-situ data

Fig. 5 presents the overall accuracy of field-measured LFMC versus estimated sub-daily LFMC from Himawari-8 AHI data (R^2=0.61, rRMSE=20.78%, p<0.05). At the sub-

daily scale, LFMC varies across days for the five sites within the fire season as illustrated in Fig. 6. Both the measured and estimated LFMC exhibit a general decreasing trend from morning to afternoon. The relatively high LFMC value observed before noon declined between 1:00 PM and 3:00 PM, but partially recovered between 3:00 and 4:00 PM on most days (Fig. 6). However, there was no decline in LFMC between 1:00 and 3:00 PM on July 31st, 2015 for the QLB site. This can be explained by the limited rainfall during that time, as evidenced by tracking the rainfall history in this area (Fig. S2). While the small amount of rainfall temporarily increased the LFMC, the intense solar radiation quickly dried out the grass. This could potentially account for the observed decline in LFMC after 14:40.

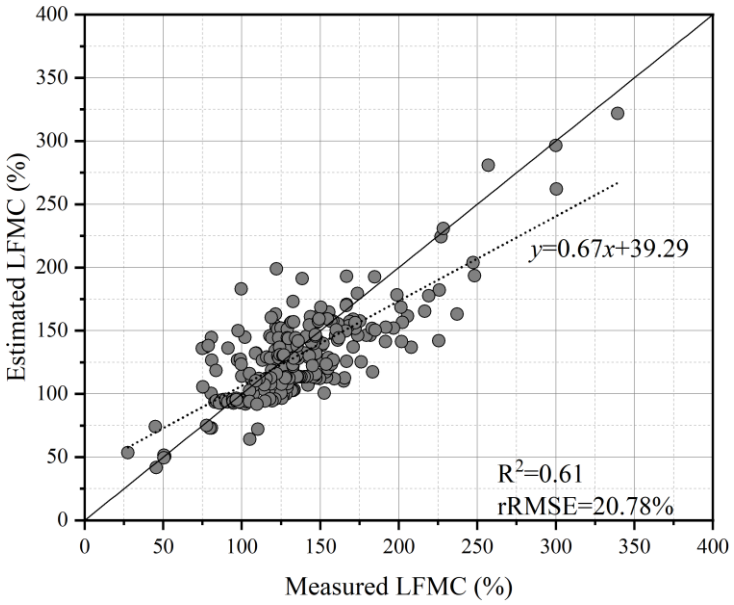

Fig. 5 LFMC field measurements versus LFMC estimations from Himawari-8 AHI data.

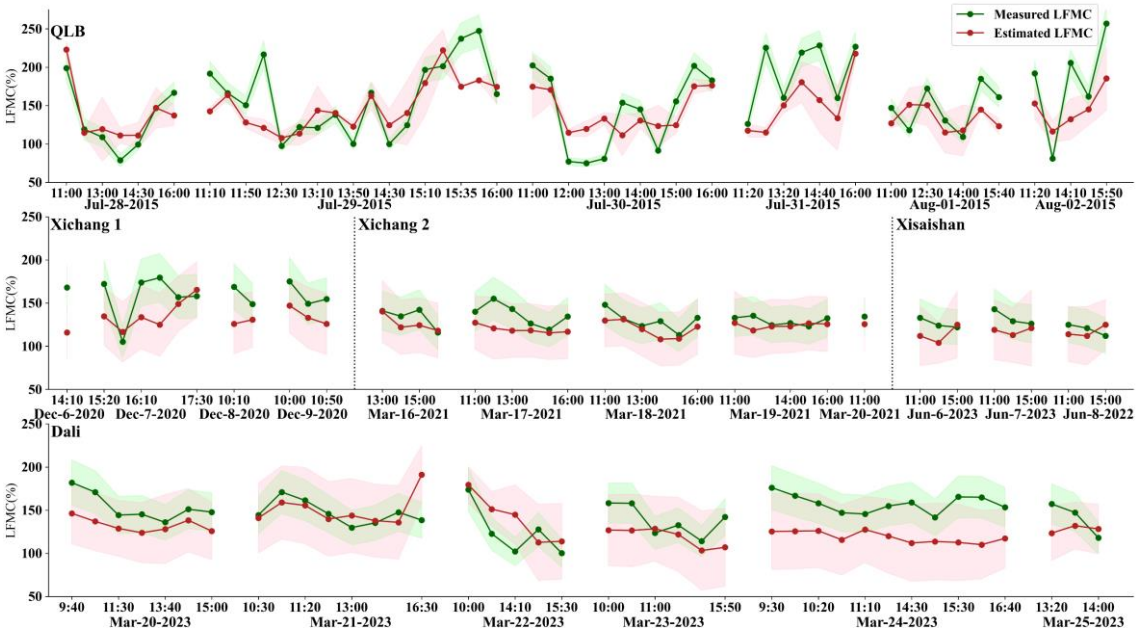

Fig. 6 Measured LFMC (green) with their standard deviation error bars (shaded green areas) versus estimated LFMC (red) from GRG-PROSAILH_5B model with their standard deviation after multiple iterations (shaded red areas) to validate sub-daily LFMC dynamics from Himawari-8 AHI at Chinese sites.

4.2 Comparison of LFMC estimates between Himawari-8 AHI, MCD43A4, and Landsat-8 OLI at daily scale

At the daily scale, a comparison of LFMC estimates between Himawari-8 AHI and MCD43A4 using a filter for site homogeneity of NDVIcv <15% revealed that the LFMC estimates from MCD43A4 had the highest accuracy (R^2=0.76, rRMSE=19.73%, p<0.05) (Fig. 7 a). The LFMC estimates from Himawari-8 AHI and resampled MCD43A4 demonstrated comparable accuracy (R^2=0.61, rRMSE=25.38%, p<0.05 and R^2=0.63, rRMSE=25.84%, p<0.05, respectively). When a more restrictive filter of $NDVI_{CV}$ < 10% for homogeneity testing was applied, the accuracy of all three cases increased (Fig. 7 b).

The accuracy increased particularly for Himawari-8 AHI (R^2: 0.61 to 0.72, and rRMSE: 25.38% to 21.57%) and resampled MCD43A4 (R^2: 0.63 to 0.75, and rRMSE: 25.84% to 22.73%) (Fig. 7 a and b). The comparison of LFMC estimates between Himawari-8 AHI and Landsat-8 OLI (Fig. 7 c and d) data showed a similar trend to that of Himawari-8 AHI and MCD43A4 data (Fig. 7 a and c). Overall, Landsat-8 OLI-based LFMC estimates achieved the highest accuracy, followed by MCD43A4 and Himawari-8AHI. However, a restrictive homogeneity test filter ($NDVI_{CV}$<10%) decreased the differences in accuracy between these three data. Finally, LFMC was consistently underestimated, with Himawari-8 AHI data showing the most significant underestimation, followed by MCD43A4 and Landsat-8 OLI (Fig. 7). This underestimation was more apparent for LFMC higher than 120%.

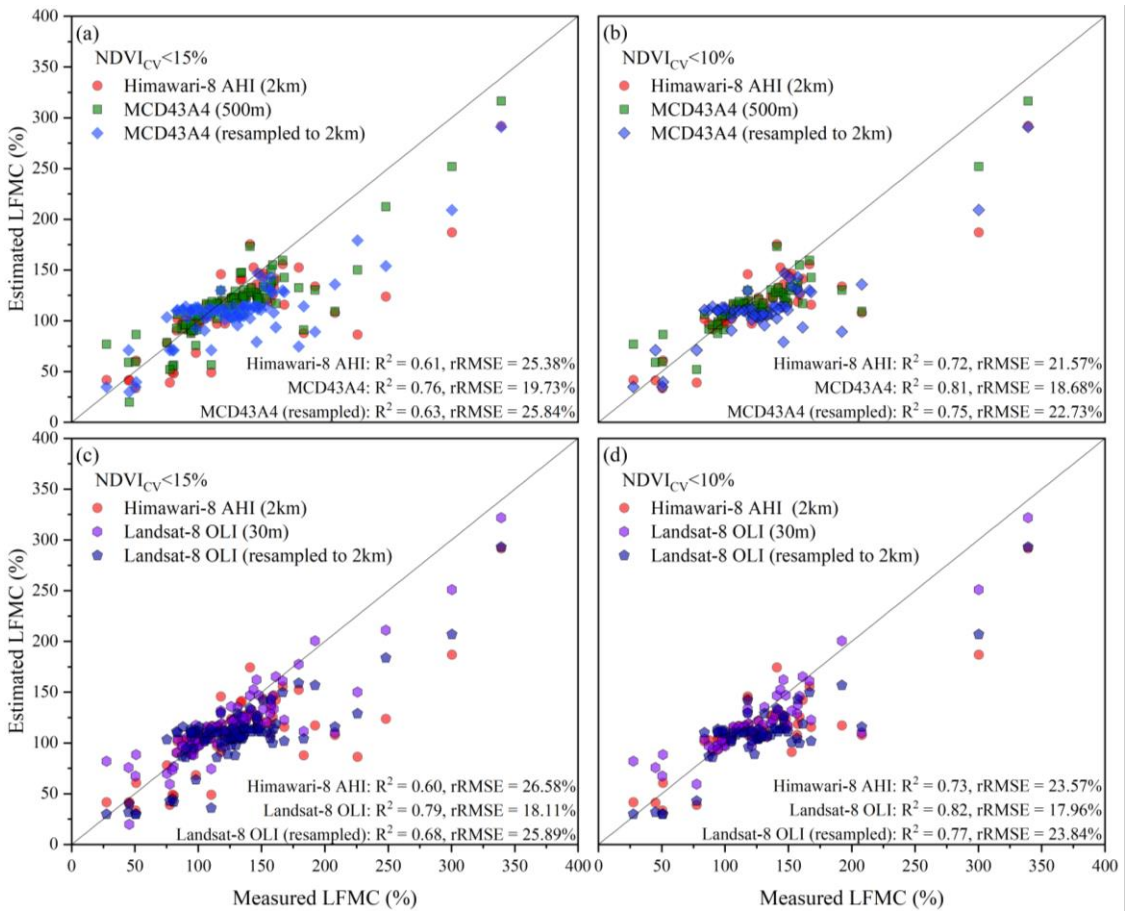

Fig. 7 Estimated versus measured LFMC based on Himawari-8 AHI, Landsat-8 OLI, and MCD43A4 across field sites in Australia and China (p<0.05). The analysis includes data using a $NDVI_{CV}$<15% (a and c) and $NDVI_{CV}$<10 % (b, and d) site homogeneity filter.

4.3 LFMC dynamics before the Queensland and Xichang wildfires

The LFMC estimates derived from Landsat-8 and MCD43A4 data further corroborated the decreasing trend in LFMC leading up to the wildfires in both Queensland and Xichang (Fig. 8 and 9). For the Queensland wildfire case (Fig. 8), the MCD43A4 LFMC product showed a modest decrease of less than <10% from an initial LFMC of 110% between August 16th and 24th, followed by a more rapid decreased of approximately 20% from August 24th to September 4th. The Landsat-8 OLI LFMC estimates were available only for August 16th and September 1st, showing a decrease of approximately 9%. When the sub-daily Himawari-8-based LFMC was averaged on a daily scale, it also exhibited a decline of around 8% during this period. Similarly, for the Xichang wildfire case (Fig. 9), LFMC estimates derived from Landsat-8 OLI, MCD43A4, and daily averaged Himawari-8 AHI data showed declines of approximately 7%, 6%, and 5%, respectively, within a 16-day period.

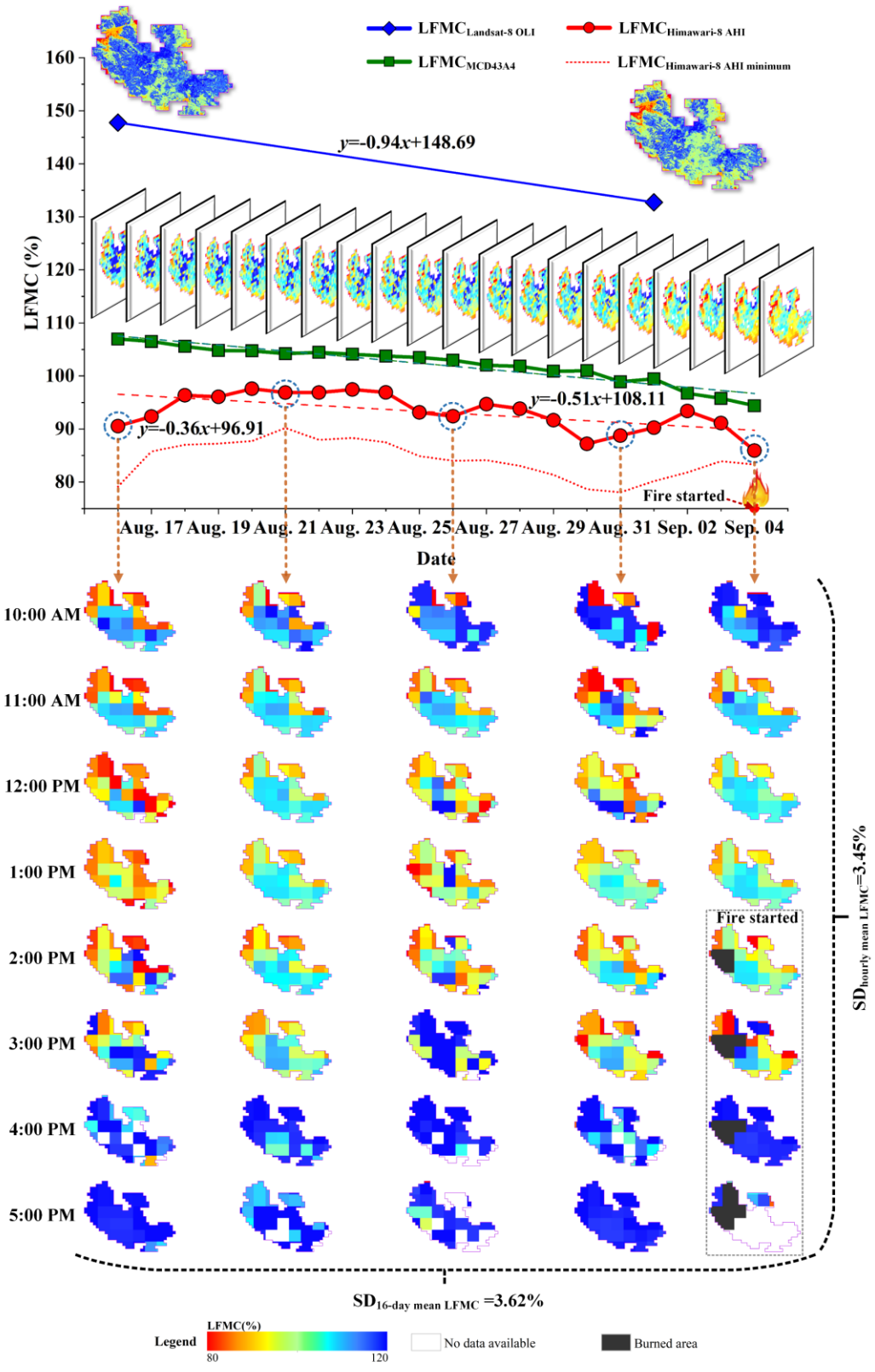

Fig. 8 Estimated averaged LFMC dynamics and trends over the Queensland wildfire in Australia from Landsat-8 OLI (blue line, 16-day scale), MCD43A4 (green line, daily

scale), mean Himawari-8 AHI (red line, sub-daily scale), and the minimum LFMC from Himawari-8 AHI (dotted red line, sub-daily scale) (top figure), as well as zoomed-in view of Himawari-8 AHI LFMC product, showing hourly intervals from August 16th to September 4th, 2019, captured every 5 days (bottom figure).

According to LFMC estimates derived from Himawari-8 AHI data collected from August 16th and September 4th, 2019, every 5 days over the Queensland wildfire region (Fig. 8), the standard deviation (SD) of the hourly mean LFMC closely resembled the LFMC variation at the 16-day scale. Specifically, the SD of the 16-day mean LFMC was found to be 3.62% while the SD of the sub-daily hourly LFMC was 3.45%. Conversely, when examining the Xichang wildfire data (Fig. 9), it became apparent that the sub-daily hourly variation of LFMC, with an SD of the hourly mean LFMC at 2.51%, was greater than the variation observed at the 16-day scale where the SD of the 16-day mean LFMC stood at 1.74%. This observation suggests that LFMC may not exhibit significant variations at the same time on different days but tends to exhibit significant fluctuations at the sub-daily scale. In both areas, LFMC typically began to decline after 10:00 AM, reaching its lowest value around 2:00 PM - 3:00 PM before gradually recovering. Notably, on September 4th, 2019, the Queensland wildfire started from the northwest region at approximately 2:00 PM, coinciding with LFMC's lowest daily value of around 95%, representing a decline of approximately 20% since 10:00 AM. Similarly, the Xichang wildfire started around 4:00 PM and saw a decrease of approximately 15% in LFMC since 10:00 AM.

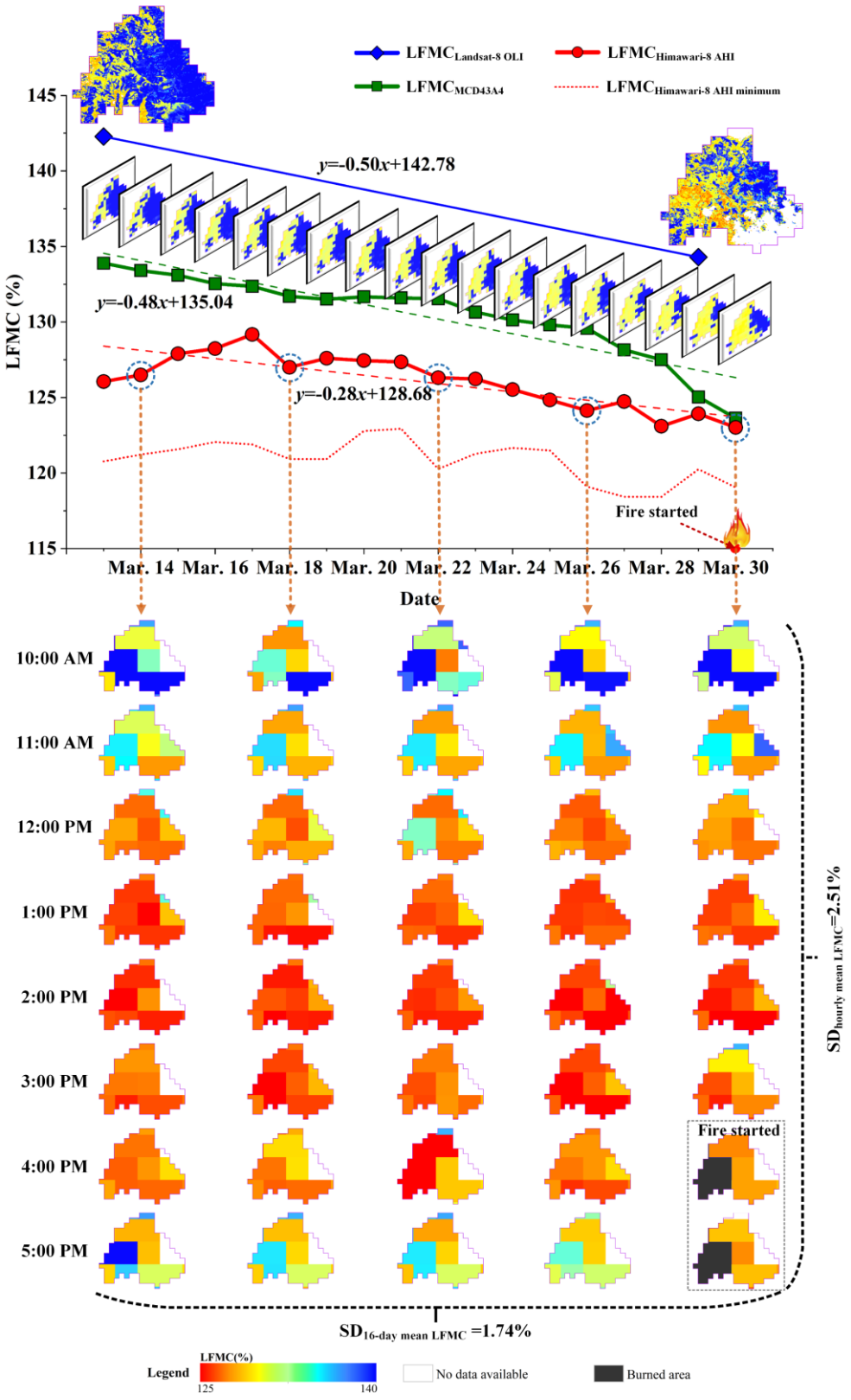

Fig. 9 Estimated averaged LFMC dynamics and trends over the Xichang wildfire in China from Landsat-8 OLI (blue line, 16-day scale), MCD43A4 (green line, daily scale), mean

Himawari-8 AHI (red line, sub-daily scale) , and the minimum LFMC from Himawari-8 AHI (dotted red line, sub-daily scale) (top figure), as well as zoomed-in view of Himawari-8 AHI LFMC product, showing hourly intervals from March 13th to 30th, 2020, captured every 5 days (bottom figure).

5. Discussion

5.1 Enhancing LFMC monitoring with sub-daily observations from Himawari-8 AHI: Implications for Wildfire Management

This study presented the first sub-daily LFMC estimation from the Himawari-8 geostationary satellite. Previous works detected sub-daily variations of vegetation water but from airborne MODIS/ASTER simulator (MASTER) (Cheng et al. 2013) and Airborne Visible/Infrared Imaging Spectrometer (AVIRIS) instrument (Cheng et al. 2014). Rather than LFMC, they estimated canopy water content (CWC) that includes LAI. In addition, LFMC depends on dry matter content, but CWC does not. These studies measured morning to afternoon declines on the ground of ~9% CWC on drip-irrigated nut tree orchards causing a ~4% decline in NDII (Cheng et al. 2013), but they did not assess natural vegetation. This study demonstrates that the sub-daily LFMC dynamics can be captured using observations from Himawari-8 at a large scale, contributing to monitoring fire danger and behavior over the course of a day.

LFMC estimations in previous literature were mainly based on polar-orbiting satellite data, such as Landsat (TM, ETM+, OLI) and MODIS products (Chuvieco et al. 2002a; García et al. 2020; Quan et al. 2017; Quan et al. 2021c; Sibanda et al. 2021; Yebra et al. 2018). Landsat-8 in combination with the new Landsat-9 improves the LFMC temporal resolution from 16 to 8 days of data (Lulla et al. 2021; Masek et al. 2020). Together with Sentinel-2A/B satellites, it is possible to estimate LFMC at 10-30 m spatial

resolution every 5 days or less, depending on the latitude (Garcia et al. 2020; Marino et al. 2020). Despite this, it is still unfeasible to capture sub-daily LFMC changes, like Himawari-8 AHI does every 10 mins. For MODIS, a morning and an afternoon product at a better spatial resolution than Himawari-8 AHI are technically possible for sub-daily LFMC monitoring, after an independent BRDF correction. Nevertheless, there are only two MODIS overpasses at daylight, from Terra satellite at ~10:30 AM and Aqua at ~1:30 PM. Therefore, such MODIS product gives limited opportunities to obtain cloud-free images in comparison to Himawari-8 AHI and misses to capture the large LFMC decay observed from 10:30 AM to 2:30 PM by Himawari-8 AHI. The short-term variation in LFMC observed in this study with Himawari-8 AHI data exceeded those observed on a daily scale, highlighting the significance of sub-daily LFMC dynamics that could potentially influence fire behavior. Furthermore, Himawari-8 AHI LFMC could take advantage of the higher spatial resolution offered by Landsat-8 OLI and MODIS by fusing with data from these sensors through spatiotemporal time series analysis (Wang and Atkinson 2018; Zhou et al. 2021).

Improved temporal LFMC estimates potentially result in better wildfire monitoring (Yebra et al. 2013; Yebra et al. 2018). Himawari-8 AHI has a relatively moderate spatial resolution (2 km), but it is still higher than the gridded meteorological data or soil moisture information used as a proxy of moisture conditions in many fire danger rating systems (Caccamo et al. 2012; Ruffault et al. 2018; Vinodkumar et al. 2021). In addition, Himawari-8 AHI is suitable for near real-time monitoring, as it has only ~30 mins latency time between satellite imaging time and the downloadable time from JMA. Instead, Landsat-8 OLI needs 15-17 days' latency time for Level-2 surface reflectance from the USGS. This delay for users to access these data makes them unrealistic for near real-time LFMC for wildfire monitoring (Wu et al. 2019). MODIS 16-day composite MCD43A4

can be built within minutes of acquisition with their direct broadcast system (https://directreadout.sci.gsfc.nasa.gov/), but there are only two daylight overpasses per day.

5.2 Challenges and considerations in sub-daily LFMC estimation using Himawari-8 AHI Data

This study demonstrates the promising potential of Himawari-8 AHI data for sub-daily LFMC estimation. However, uncertainties are inherent in this database. For example, variations in solar zenith angles, particularly in the early morning and late afternoon (Fig. 8 and 9). Despite efforts were made to account for the dynamic interplay between solar angles, scene geometry, and sensor observations in the acquisition of Himawari-8 AHI reflectance data, changes in solar angles still impact LFMC estimates by altering the proportion of shadow cast in the scene. However, it is important to note that the influence of solar angle variation on LFMC estimates is relatively minor compared to the pronounced sub-daily LFMC fluctuations. These sub-daily variations in LFMC may be attributed to the daily maximal vapor pressure defect (VPD), which triggers elevated transpiration rates (Griebel et al. 2023; Griebel et al. 2020; Griebel et al. 2022; Sun et al. 2010). In other words, during periods of maximum VPD, there are short-term declines in LFMC, followed by a subsequent recovery. This midday decrease and subsequent water potential recovery is well documented in the plant physiology literature (Griebel et al. 2022; Nolan et al. 2022; Nolan et al. 2018; Sun et al. 2010). Additionally, it is worth noting that weather conditions can also influence LFMC variations, but this relationship is non-linear and intricate. This complexity is particularly evident in regions with diverse climate patterns, vegetation species, and geographical conditions, as is the case in this study (Fig. S3).

The wide view angles of the Himawari-8 satellite, especially in areas such as western China, may introduce uncertainty in estimating LFMC, partly caused by the varying spatial size of the AHI pixel. However, this issue can be effectively mitigated by leveraging the Himawari-8 L1 Gridded data obtained from the AHI. This data has undergone official resampling procedures to ensure equal latitude-longitude grids and a spatial resolution at a nadir of approximately 0.02° (~2 km). Moreover, the selected sites typically have an area larger than 2 km × 2 km, especially in western China, to ensure the complete location of the AHI pixel within the site area, and maintain consistent species, weather conditions, and terrain characteristics within each site (section 2.1). Additionally, this study has thoroughly taken into account the geometric observation parameters within the PROSAILH RTM during the reflectance modelling phase. This RTM has been widely used for simulating BRDF, enhancing our ability to address geometric considerations. To comprehensively explore the impact of geometric observation on LFMC estimation, ongoing research is currently underway to compare LFMC estimates obtained from both Himawari-8 and Geostationary Korea Multi-Purpose Satellite-2A (GK-2A). Although these two geostationary satellites possess similar spectral configurations, they significantly differ in terms of their view angles. Specifically, Himawari-8 operates at approximately 140.7° E, and the GK-2A operates at around 128.2° E. This combination of shared spectral configuration characteristics and divergent viewing angles positions these satellites as ideal candidates for a detailed investigation into the impact of geometric observation on LFMC estimation.

The heterogeneity within the coarse spatial resolution of the Himawari-8 AHI pixel also affected the validation accuracy. Sampling sites with highly heterogeneous vegetation were excluded at the 2 km Himawari-8 AHI spatial resolution based on Landsat-8 OLI when $NDVI_{CV}$ > 15%, but the effect of heterogeneity still persisted. This

was demonstrated by the higher LFMC accuracy of 30 m Landsat-8 OLI and 500 m MCD43A4 data compared to the 2 km Himawari-8 AHI (Fig. 7). When the Landsat-8 OLI and MCD43A4 data were resampled to a 2 km scale to match the Himawari-8 AHI, the accuracy of LFMC estimates decreased. Moreover, by applying $NDVI_{CV}$ < 10%, the LFMC estimate increased for all these data, and the accuracy difference between these three data sets became smaller as more homogeneous vegetation leads to better LFMC estimations (Chuvieco et al. 2002b).

5.3 Enhancing wildfire risk assessment with sub-daily LFMC and its role in the fire environment

Three pivotal factors are essential for understanding the wildfire risk: topography, weather, and fuel; collectively shaped by the 'fire environment triangle' (Countryman 1972; Pyne et al. 1996). In addition to this, ignition sources like lighting and human activities significantly contribute to wildfire occurrences (Abatzoglou and Williams 2016; Andela et al. 2017; Chuvieco et al. 2021; Parisien et al. 2016). LFMC serves as a crucial component in forecasting ignition potential, while lower LFMC values indicate a higher wildfire potential (Rao et al. 2023; Yebra et al. 2013; Yebra et al. 2018). Quan et al. (2021b) previously modelled wildfire risk for China by considering daily MCD43A4-derived LFMC data, but a higher temporal resolution in LFMC mapping offers distinct advantages for proactive wildfire risk assessment. With the sub-daily LFMC data presented in this study, there is the potential to enhance the wildfire danger assessment from a daily to a finely detailed sub-daily hourly scale.

6. Conclusion

This study presented a novel approach, combining the GRG method and RTM, to achieve sub-daily LFMC estimations from Himawari-8 AHI data. The method effectively addressed the challenges posed by dynamic sun-target-sensor geometry and ill-posed RTM inversion, enhancing the accuracy of LFMC estimations. Field LFMC measurements conducted in China validated the sub-daily Himawari-8 AHI LFMC estimations, demonstrating reasonable accuracy. Comparison with other satellite products at the inter-daily scale yielded promising results, highlighting the potential of Himawari-8 AHI LFMC data for wildfire risk assessment and behavior prediction. The GRG-RTM approach adopted here not only accelerated convergence, but also improved inversion accuracy for the LFMC estimations. Himawari-8 AHI's continuous and near real-time data stream provides sub-daily LFMC information for wildfire risk and behavior assessment. While the Himawari-8 AHI LFMC product rendered similar performance in comparison to other inter-daily satellite products and also reasonable agreement with field LFMC data, further validation across broader geographic scales is recommended to ensure its applicability at the continental scale.

Acknowledgments

The National Key R&D Program of China (2022YFC3003001) and National Natural Science Foundation of China (Contract No. U20A2090 and 41801272) supported this work. The authors are grateful for the exhaustive field sampling work completed by Gengke Lai, Chunquan Fan, Yanxi Li, Jianpeng Ying, Lin Chen, and Tengfei Xiao.

References

Abatzoglou, J.T., & Williams, A.P. (2016). Impact of anthropogenic climate change on wildfire across western US forests. *Proc Natl Acad Sci U S A, 113*, 11770-11775

Andela, N., Morton, D.C., Giglio, L., Chen, Y., van der Werf, G.R., Kasibhatla, P.S., DeFries, R.S., Collatz, G.J., Hantson, S., Kloster, S., Bachelet, D., Forrest, M., Lasslop, G., Li, F., Mangeon, S., Melton, J.R., Yue, C., & Randerson, J.T. (2017). A human-driven decline in global burned area. *Science, 356*, 1356-1362

Argañaraz, J.P., Gavier Pizarro, G., Zak, M., Landi, M.A., & Bellis, L.M. (2015). Human and biophysical drivers of fires in Semiarid Chaco mountains of Central Argentina. *Science of The Total Environment, 520*, 1-12

Arganaraz, J.P., Landi, M.A., Bravo, S.J., Gavier-Pizarro, G.I., Scavuzzo, C.M., & Bellis, L.M. (2016). Estimation of Live Fuel Moisture Content From MODIS Images for Fire Danger Assessment in Southern Gran Chaco. *Ieee Journal of Selected Topics in Applied Earth Observations and Remote Sensing, 9*, 5339-5349

Bilal, M., Nazeer, M., Nichol, J.E., Bleiweiss, M.P., Qiu, Z.F., Jakel, E., Campbell, J.R., Atique, L., Huang, X.L., & Lolli, S. (2019). A Simplified and Robust Surface Reflectance Estimation Method (SREM) for Use over Diverse Land Surfaces Using Multi-Sensor Data. *Remote Sensing, 11*, 24

Bowman, D., Williamson, G., Yebra, M., Lizundia-Loiola, J., Pettinari, M.L., Shah, S., Bradstock, R., & Chuvieco, E. (2020). Wildfires: Australia needs national monitoring agency. *Nature, 584*, 188-191

Bowyer, P., & Danson, F.M. (2004). Sensitivity of spectral reflectance to variation in live fuel moisture content at leaf and canopy level. *Remote Sensing of Environment, 92*, 297-308

Caccamo, G., Chisholm, L.A., Bradstock, R.A., Puotinen, M.L., & Pippen, B.G. (2012). Monitoring live fuel moisture content of heathland, shrubland and sclerophyll forest in south-eastern Australia using MODIS data. *International Journal of Wildland Fire, 21*, 257

Cao, X., Cui, X.H., Yue, M., Chen, J., Tanikawa, H., & Ye, Y. (2013). Evaluation of wildfire propagation susceptibility in grasslands using burned areas and multivariate logistic regression. *International Journal of Remote Sensing, 34*, 6679-6700

Casas, A., Riaño, D., Ustin, S.L., Dennison, P., & Salas, J. (2014). Estimation of water-related biochemical and biophysical vegetation properties using multitemporal airborne hyperspectral data and its comparison to MODIS spectral response. *Remote Sensing of Environment, 148*, 28-41

Cheng, T., Riano, D., Koltunov, A., Whiting, M.L., Ustin, S.L., & Rodriguez, J. (2013). Detection of diurnal variation in orchard canopy water content using MODIS/ASTER airborne simulator (MASTER) data. *Remote Sensing of Environment, 132*, 1-12

Cheng, T., Riaño, D., & Ustin, S.L. (2014). Detecting diurnal and seasonal variation in canopy water content of nut tree orchards from airborne imaging spectroscopy data using continuous wavelet analysis. *Remote Sensing of Environment, 143*, 39-53

Cheng, Y.-B., Zarco-Tejada, P.J., Riano, D., Rueda, C.A., & Ustin, S.L. (2006). Estimating vegetation water content with hyperspectral data for different canopy scenarios: Relationships between AVIRIS and MODIS indexes. *Remote Sensing of Environment, 105*, 354-366

Chuvieco, E., Aguado, I., Yebra, M., Nieto, H., Salas, J., Martín, M.P., Vilar, L., Martínez, J., Martín, S., Ibarra, P., de la Riva, J., Baeza, J., Rodríguez, F., Molina, J.R., Herrera, M.A., & Zamora, R. (2010). Development of a framework for fire risk assessment using remote sensing and geographic information system technologies. *Ecological Modelling, 221*, 46-58

Chuvieco, E., Pettinari, M.L., Koutsias, N., Forkel, M., Hantson, S., & Turco, M. (2021). Human and climate drivers of global biomass burning variability. *Science of The Total Environment*

Chuvieco, E., Riano, D., Aguado, I., & Cocero, D. (2002a). Estimation of fuel moisture content from multitemporal analysis of Landsat Thematic Mapper reflectance data: applications in fire danger assessment. *International Journal of Remote Sensing, 23*, 2145-2162

Chuvieco, E., Riaño, D., Aguado, I., & Cocero, D. (2002b). Estimation of fuel moisture content from multitemporal analysis of Landsat Thematic Mapper reflectance data: applications in fire danger assessment. *International Journal of Remote Sensing, 23*, 2145-2162

Collins, L., Bradstock, R.A., Clarke, H., Clarke, M.F., Nolan, R.H., & Penman, T.D. (2021). The 2019/2020 mega-fires exposed Australian ecosystems to an unprecedented extent of high-severity fire. *Environmental Research Letters, 16*

Countryman, C.M. (1972). *The fire environment concept*. Pacific Southwest Forest and Range Experiment Station

Estevez, J., Vicent, J., Rivera-Caicedo, J.P., Morcillo-Pallares, P., Vuolo, F., Sabater, N., Camps-Valls, G., Moreno, J., & Verrelst, J. (2020). Gaussian processes retrieval of LAI from Sentinel-2 top-of-atmosphere radiance data. *Isprs Journal of Photogrammetry and Remote Sensing, 167*, 289-304

Fan, L., Wigneron, J.P., Xiao, Q., Al-Yaari, A., Wen, J., Martin-StPaul, N., Dupuy, J.L., Pimont, F., Al Bitar, A., Fernandez-Moran, R., & Kerr, Y.H. (2018). Evaluation of microwave remote sensing for monitoring live fuel moisture content in the Mediterranean region. *Remote Sensing of Environment, 205*, 210-223

Fang, H., Liang, S., & Kuusk, A. (2003). Retrieving leaf area index using a genetic algorithm with a canopy radiative transfer model. *Remote Sensing of Environment, 85*, 257-270

Feret, J.B., Francois, C., Asner, G.P., Gitelson, A.A., Martin, R.E., Bidel, L.P.R., Ustin, S.L., le Maire, G., & Jacquemoud, S. (2008). PROSPECT-4 and 5: Advances in the leaf optical properties model separating photosynthetic pigments. *Remote Sensing of Environment, 112*, 3030-3043

Garcia, M., Chuvieco, E., Nieto, H., & Aguado, I. (2008). Combining AVHRR and meteorological data for estimating live fuel moisture content. *Remote Sensing of Environment, 112*, 3618-3627

Garcia, M., Riano, D., Yebra, M., Salas, J., Cardil, A., Monedero, S., Ramirez, J., Martin, M.P., Vilar, L., Gajardo, J., & Ustin, S. (2020). A Live Fuel Moisture Content Product from Landsat TM Satellite Time Series for Implementation in Fire Behavior Models. *Remote Sensing, 12*, 15

García, M., Riaño, D., Yebra, M., Salas, J., Cardil, A., Monedero, S., Ramirez, J., Martín, M.P., Vilar, L., Gajardo, J., & Ustin, S. (2020). A Live Fuel Moisture Content Product from Landsat TM Satellite Time Series for Implementation in Fire Behavior Models. *Remote Sensing, 12*, 1714

Gill, A., WSW, T., & MAC ARTHUR, D. (1978). Role of moisture in the flammability of natural fuels in the laboratory

Griebel, A., Boer, M.M., Blackman, C., Choat, B., Ellsworth, D.S., Madden, P., Medlyn, B., Resco de Dios, V., Wujeska-Klause, A., Yebra, M., Younes Cardenas, N., & Nolan, R.H. (2023). Specific leaf area and vapour pressure deficit control live fuel moisture content. *Functional Ecology, 37*, 719-731

Griebel, A., Metzen, D., Boer, M.M., Barton, C.V., Renchon, A.A., Andrews, H.M., & Pendall, E. (2020). Using a paired tower approach and remote sensing to assess carbon sequestration and energy distribution in a heterogeneous sclerophyll forest. *Science of The Total Environment, 699*, 133918

Griebel, A., Peters, J.M., Metzen, D., Maier, C., Barton, C.V., Speckman, H.N., Boer, M.M., Nolan, R.H., Choat, B., & Pendall, E. (2022). Tapping into the physiological responses to mistletoe infection during heat and drought stress. *Tree Physiology, 42*, 523-536

Grootemaat, S., Wright, I.J., van Bodegom, P.M., Cornelissen, J.H., & Cornwell, W.K. (2015). Burn or rot: leaf traits explain why flammability and decomposability are decoupled across species. *Functional Ecology*, *29*, 1486-1497

Hosgood, B., Jacquemoud, S., Andreoli, G., Verdebout, J., Pedrini, G., & Schmuck, G. (1995). Leaf optical properties experiment 93 (LOPEX93). *Ispra Italy'European Commission, Joint Research Centre Institute of Remote Sensing Applications*

Ishimoto, H., Masuda, K., Mano, Y., Orikasa, N., & Uchiyama, A. (2012). Irregularly shaped ice aggregates in optical modeling of convectively generated ice clouds. *Journal of Quantitative Spectroscopy and Radiative Transfer, 113*, 632-643

Ishimoto, H., Masuda, K., Mano, Y., Orikasa, N., & Uchiyama, A. (2013). Optical modeling of irregularly shaped ice particles in convective cirrus. In, *AIP Conference Proceedings* (pp. 184-187): American Institute of Physics

Jacquemoud, S., & Baret, F. (1990). PROSPECT: A model of leaf optical properties spectra. *Remote Sensing of Environment, 34*, 75-91

Jeong, S., Ryu, Y., Dechant, B., Li, X., Kong, J., Choi, W., Kang, M., Yeom, J., Lim, J., Jang, K., & Chun, J. (2023). Tracking diurnal to seasonal variations of gross primary productivity using a geostationary satellite, GK-2A advanced meteorological imager. *Remote Sensing of Environment, 284*

Jia, S.Y., Kim, S.H., Nghiem, S.V., & Kafatos, M. (2019). Estimating Live Fuel Moisture Using SMAP L-Band Radiometer Soil Moisture for Southern California, USA. *Remote Sensing, 11*

John, M., Osterman, J., & Mitchell, J. (1995). Calibration of the Minolta SPAD-502 leaf chlorophyll meter. *Photosynthesis Research: An International Journal*

Johnston, F.H., Borchers-Arriagada, N., Morgan, G.G., Jalaludin, B., Palmer, A.J., Williamson, G.J., & Bowman, D.M. (2020). Unprecedented health costs of smoke-related PM 2.5 from the 2019–20 Australian megafires. *Nature Sustainability*, 1-6

Jolly, W.M., Cochrane, M.A., Freeborn, P.H., Holden, Z.A., Brown, T.J., Williamson, G.J., & Bowman, D. (2015). Climate-induced variations in global wildfire danger from 1979 to 2013. *Nature Communications, 6*, 11

Jurdao, S., Chuvieco, E., & Arevalillo, J.M. (2012). Modelling Fire Ignition Probability from Satellite Estimates of Live Fuel Moisture Content. *Fire Ecology, 8*, 77-97

Jurdao, S., Yebra, M., Guerschman, J.P., & Chuvieco, E. (2013). Regional estimation of woodland moisture content by inverting Radiative Transfer Models. *Remote Sensing of Environment, 132*, 59-70

Khan, A.M., Stoy, P.C., Douglas, J.T., Anderson, M., Diak, G., Otkin, J.A., Hain, C., Rehbein, E.M., & McCorkel, J. (2021). Reviews and syntheses: Ongoing and emerging opportunities to improve environmental science using observations from

the Advanced Baseline Imager on the Geostationary Operational Environmental Satellites. *Biogeosciences, 18*, 4117-4141

Kuusk, A. (1991). *The Hot Spot Effect in Plant Canopy Reflectance*. Springer Berlin Heidelberg

Letu, H., Ishimoto, H., Riedi, J., Nakajima, T.Y., C.-Labonnote, L., Baran, A.J., Nagao, T.M., & Sekiguchi, M. (2016). Investigation of ice particle habits to be used for ice cloud remote sensing for the GCOM-C satellite mission. *Atmospheric Chemistry and Physics, 16*, 12287-12303

Letu, H., Nagao, T.M., Nakajima, T.Y., & Matsumae, Y. (2014). Method for validating cloud mask obtained from satellite measurements using ground-based sky camera. *Applied Optics, 53*, 7523-7533

Letu, H., Nagao, T.M., Nakajima, T.Y., Riedi, J., Ishimoto, H., Baran, A.J., Shang, H., Sekiguchi, M., & Kikuchi, M. (2019). Ice Cloud Properties From Himawari-8/AHI Next-Generation Geostationary Satellite: Capability of the AHI to Monitor the DC Cloud Generation Process. *Ieee Transactions on Geoscience and Remote Sensing, 57*, 3229-3239

Letu, H., Nakajima, T.Y., & Matsui, T.N. (2012). Development of an ice crystal scattering database for the global change observation mission/second generation global imager satellite mission: investigating the refractive index grid system and potential retrieval error. *Applied Optics, 51*, 6172-6178

Lulla, K., Nellis, M.D., Rundquist, B., Srivastava, P.K., & Szabo, S. (2021). Mission to earth: LANDSAT 9 will continue to view the world. *Geocarto International, 36*, 2261-2263

Luo, Y., El-Madany, T.S., Filippa, G., Ma, X., Ahrens, B., Carrara, A., Gonzalez-Cascon, R., Cremonese, E., Galvagno, M., Hammer, T.W., Pacheco-Labrador, J., Martín, M.P., Moreno, G., Perez-Priego, O., Reichstein, M., Richardson, A.D., Römermann, C., & Migliavacca, M. (2018). Using Near-Infrared-Enabled Digital Repeat Photography to Track Structural and Physiological Phenology in Mediterranean Tree–Grass Ecosystems. *Remote Sensing, 10*

Marino, E., Yebra, M., Guillen-Climent, M., Algeet, N., Tome, J.L., Madrigal, J., Guijarro, M., & Hernando, C. (2020). Investigating Live Fuel Moisture Content Estimation in Fire-Prone Shrubland from Remote Sensing Using Empirical Modelling and RTM Simulations. *Remote Sensing, 12*, 19

Masek, J.G., Wulder, M.A., Markham, B., McCorkel, J., Crawford, C.J., Storey, J., & Jenstrom, D. (2020). Landsat 9: Empowering open science and applications through continuity. *Remote Sensing of Environment, 248*

Masuda, K., Ishimoto, H., & Mano, Y. (2012). Short Note Efficient method of computing a geometric optics integral for light scattering by nonspherical particles. *Papers in Meteorology and Geophysics, 63*, 15-19

Matthews, S. (2010). Effect of drying temperature on fuel moisture content measurements. *International Journal of Wildland Fire, 19*, 800

Miller, L., Zhu, L., Yebra, M., Rüdiger, C., & Webb, G.I. (2022). Multi-modal temporal CNNs for live fuel moisture content estimation. *Environmental Modelling & Software*, 105467

Moritz, M.A., Parisien, M.-A., Batllori, E., Krawchuk, M.A., Van Dorn, J., Ganz, D.J., & Hayhoe, K. (2012). Climate change and disruptions to global fire activity. *Ecosphere, 3*, 1-22

Myneni, R.B., Hoffman, S., Knyazikhin, Y., Privette, J.L., Glassy, J., Tian, Y., Wang, Y., Song, X., Zhang, Y., Smith, G.R., Lotsch, A., Friedl, M., Morisette, J.T., Votava, P.,

Nemani, R.R., & Running, S.W. (2002). Global products of vegetation leaf area and fraction absorbed PAR from year one of MODIS data. *Remote Sensing of Environment, 83*, 214-231

Myoung, B., Kim, S.H., Nghiem, S.V., Jia, S.Y., Whitney, K., & Kafatos, M.C. (2018). Estimating Live Fuel Moisture from MODIS Satellite Data for Wildfire Danger Assessment in Southern California USA. *Remote Sensing, 10*, 17

Nakajima, T.Y., Tsuchiya, T., Ishida, H., Matsui, T.N., & Shimoda, H. (2011). Cloud detection performance of spaceborne visible-to-infrared multispectral imagers. *Applied Optics, 50*, 2601-2616

Nolan, R.H., Boer, M.M., Collins, L., Resco de Dios, V., Clarke, H., Jenkins, M., Kenny, B., & Bradstock, R.A. (2020). Causes and consequences of eastern Australia's 2019–20 season of mega-fires. *Global Change Biology, 26*, 1039-1041

Nolan, R.H., Boer, M.M., Resco de Dios, V., Caccamo, G., & Bradstock, R.A. (2016). Large-scale, dynamic transformations in fuel moisture drive wildfire activity across southeastern Australia. *Geophysical Research Letters, 43*, 4229-4238

Nolan, R.H., Foster, B., Griebel, A., Choat, B., Medlyn, B.E., Yebra, M., Younes, N., & Boer, M.M. (2022). Drought-related leaf functional traits control spatial and temporal dynamics of live fuel moisture content. *Agricultural and Forest Meteorology, 319*

Nolan, R.H., Hedo, J., Arteaga, C., Sugai, T., & Resco de Dios, V. (2018). Physiological drought responses improve predictions of live fuel moisture dynamics in a Mediterranean forest. *Agricultural and Forest Meteorology, 263*, 417-427

Parisien, M.-A., Miller, C., Parks, S.A., DeLancey, E.R., Robinne, F.-N., & Flannigan, M.D. (2016). The spatially varying influence of humans on fire probability in North America. *Environmental Research Letters, 11*, 075005

Pyne, S.J., Andrews, P.L., & Laven, R.D. (1996). *Introduction to wildland fire*. John Wiley and Sons

Qin, J., Liang, S., Li, X., & Wang, J. (2008). Development of the Adjoint Model of a Canopy Radiative Transfer Model for Sensitivity Study and Inversion of Leaf Area Index. *IEEE Transactions on Geoscience & Remote Sensing, 46*, 2028-2037

Quan, X., He, B., & Li, X. (2015). A Bayesian Network-Based Method to Alleviate the Ill-Posed Inverse Problem: A Case Study on Leaf Area Index and Canopy Water Content Retrieval. *Ieee Transactions on Geoscience and Remote Sensing, 53*, 6507-6517

Quan, X., He, B., Yebra, M., Yin, C., Liao, Z., & Li, X. (2017). Retrieval of forest fuel moisture content using a coupled radiative transfer model. *Environmental Modelling & Software, 95*, 290-302

Quan, X., Li, Y., He, B., Cary, G.J., & Lai, G. (2021a). Application of Landsat ETM+ and OLI Data for Foliage Fuel Load Monitoring Using Radiative Transfer Model and Machine Learning Method. *IEEE Journal of Selected Topics in Applied Earth Observations and Remote Sensing, 14*, 5100-5110

Quan, X., Wang, W., Xie, Q., He, B., Resco de Dios, V., Yebra, M., Jiao, M., & Chen, R. (2023). Improving wildfire occurrence modelling by integrating time-series features of weather and fuel moisture content. *Environmental Modelling & Software, 170*

Quan, X., Xie, Q., He, B., Luo, K., & Liu, X. (2021b). Integrating remotely sensed fuel variables into wildfire danger assessment for China. *International Journal of Wildland Fire, 30*, 807-821

Quan, X., Yebra, M., Riaño, D., He, B., Lai, G., & Liu, X. (2021c). Global fuel moisture content mapping from MODIS. *International Journal of Applied Earth Observation and Geoinformation, 101*

Rao, K., Williams, A.P., Diffenbaugh, N.S., Yebra, M., Bryant, C., & Konings, A.G. (2023). Dry Live Fuels Increase the Likelihood of Lightning-Caused Fires. *Geophysical Research Letters, 50*, e2022GL100975

Rao, K., Williams, A.P., Flefil, J.F., & Konings, A.G. (2020). SAR-enhanced mapping of live fuel moisture content. *Remote Sensing of Environment, 245*, 111797

Resco de Dios, V., Hedo, J., Cunill Camprubi, A., Thapa, P., Martinez Del Castillo, E., Martinez de Aragon, J., Bonet, J.A., Balaguer-Romano, R., Diaz-Sierra, R., Yebra, M., & Boer, M.M. (2021). Climate change induced declines in fuel moisture may turn currently fire-free Pyrenean mountain forests into fire-prone ecosystems. *Sci Total Environ, 797*, 149104

Riaño, D., Vaughan, P., Chuvieco, E., Zarco-Tejada, P.J., & Ustin, S.L. (2005). Estimation of fuel moisture content by inversion of radiative transfer models to simulate equivalent water thickness and dry matter content: analysis at leaf and canopy level. *Ieee Transactions on Geoscience and Remote Sensing, 43*, 819-826

Richter, K., Atzberger, C., Hank, T.B., & Mauser, W. (2012). Derivation of biophysical variables from Earth observation data: validation and statistical measures. *Journal of Applied Remote Sensing, 6*, 063557-063557

Ruffault, J., Martin-StPaul, N., Pimont, F., & Dupuy, J.-L. (2018). How well do meteorological drought indices predict live fuel moisture content (LFMC)? An assessment for wildfire research and operations in Mediterranean ecosystems. *Agricultural and Forest Meteorology, 262*, 391-401

Schaaf, C.B., Gao, F., Strahler, A.H., Lucht, W., Li, X., Tsang, T., Strugnell, N.C., Zhang, X., Jin, Y., & Muller, J.-P. (2002). First operational BRDF, albedo nadir reflectance products from MODIS. *Remote Sensing of Environment, 83*, 135-148

Sibanda, M., Onisimo, M., Dube, T., & Mabhaudhi, T. (2021). Quantitative assessment of grassland foliar moisture parameters as an inference on rangeland condition in the mesic rangelands of southern Africa. *International Journal of Remote Sensing, 42*, 1474-1491

Sun, W., Resco, V., & Williams, D.G. (2010). Nocturnal and seasonal patterns of carbon isotope composition of leaf dark-respired carbon dioxide differ among dominant species in a semiarid savanna. *Oecologia, 164*, 297-310

Tanase, M.A., Panciera, R., Lowell, K., & Aponte, C. (2015). Monitoring live fuel moisture in semiarid environments using L-band radar data. *International Journal of Wildland Fire, 24*, 560-572

Verhoef, W. (1984). Light scattering by leaf layers with application to canopy reflectance modeling: The SAIL model. *Remote Sensing of Environment, 16*, 125-141

Vinodkumar, V., Dharssi, I., Yebra, M., & Fox-Hughes, P. (2021). Continental-scale prediction of live fuel moisture content using soil moisture information. *Agricultural and Forest Meteorology, 307*, 108503

Wang, L., Quan, X.W., He, B.B., Yebra, M., Xing, M.F., & Liu, X.Z. (2019). Assessment of the Dual Polarimetric Sentinel-1A Data for Forest Fuel Moisture Content Estimation. *Remote Sensing, 11*

Wang, L.L., Hunt, E.R., Qu, J.J., Hao, X.J., & Daughtry, C.S.T. (2013). Remote sensing of fuel moisture content from ratios of narrow-band vegetation water and dry-matter indices. *Remote Sensing of Environment, 129*, 103-110

Wang, Q., & Atkinson, P.M. (2018). Spatio-temporal fusion for daily Sentinel-2 images. *Remote Sensing of Environment, 204*, 31-42

Ward, M., Tulloch, A.I., Radford, J.Q., Williams, B.A., Reside, A.E., Macdonald, S.L., Mayfield, H.J., Maron, M., Possingham, H.P., & Vine, S.J. (2020). Impact of 2019–2020 mega-fires on Australian fauna habitat. *Nature Ecology & Evolution*, 1-6

Wu, Z.T., Snyder, G., Vadnais, C., Arora, R., Babcock, M., Stensaas, G., Doucette, P., & Newman, T. (2019). User needs for future Landsat missions. *Remote Sensing of Environment, 231*

Xiao, J., Fisher, J.B., Hashimoto, H., Ichii, K., & Parazoo, N.C. (2021). Emerging satellite observations for diurnal cycling of ecosystem processes. *Nature Plants, 7*, 877-887

Yebra, M., & Chuvieco, E. (2009). Linking ecological information and radiative transfer models to estimate fuel moisture content in the Mediterranean region of Spain: Solving the ill-posed inverse problem. *Remote Sensing of Environment, 113*, 2403-2411

Yebra, M., Chuvieco, E., & Riaño, D. (2008). Estimation of live fuel moisture content from MODIS images for fire risk assessment. *Agricultural and Forest Meteorology, 148*, 523-536

Yebra, M., Dennison, P.E., Chuvieco, E., Riaño, D., Zylstra, P., Hunt, E.R., Danson, F.M., Qi, Y., & Jurdao, S. (2013). A global review of remote sensing of live fuel moisture content for fire danger assessment: Moving towards operational products. *Remote Sensing of Environment, 136*, 455-468

Yebra, M., Quan, X., Riaño, D., Rozas Larraondo, P., van Dijk, A.I.J.M., & Cary, G.J. (2018). A fuel moisture content and flammability monitoring methodology for continental Australia based on optical remote sensing. *Remote Sensing of Environment, 212*, 260-272

Yebra, M., Scortechini, G., Badi, A., Beget, M.E., Boer, M.M., Bradstock, R., Chuvieco, E., Danson, F.M., Dennison, P., de Dios, V.R., Di Bella, C.M., Forsyth, G., Frost, P., Garcia, M., Hamdi, A., He, B.B., Jolly, M., Kraaij, T., Martin, M.P., Mouillot, F., Newnham, G., Nolan, R.H., Pellizzaro, G., Qi, Y., Quan, X.W., Riano, D., Roberts, D., Sow, M., & Ustin, S. (2019a). Globe-LFMC, a global plant water status database for vegetation ecophysiology and wildfire applications. *Scientific Data, 6*, 8

Yebra, M., Scortechini, G., Badi, A., Beget, M.E., Boer, M.M., Bradstock, R., Chuvieco, E., Danson, F.M., Dennison, P., Resco de Dios, V., Di Bella, C.M., Forsyth, G., Frost, P., Garcia, M., Hamdi, A., He, B., Jolly, M., Kraaij, T., Martin, M.P., Mouillot, F., Newnham, G., Nolan, R.H., Pellizzaro, G., Qi, Y., Quan, X., Riano, D., Roberts, D., Sow, M., & Ustin, S. (2019b). Globe-LFMC, a global plant water status database for vegetation ecophysiology and wildfire applications. *Sci Data, 6*, 155

Youngentob, K.N., Zdenek, C., & van Gorsel, E. (2016). A simple and effective method to collect leaves and seeds from tall trees. *Methods in Ecology and Evolution, 7*, 1119-1123

Zhou, J., Chen, J., Chen, X., Zhu, X., Qiu, Y., Song, H., Rao, Y., Zhang, C., Cao, X., & Cui, X. (2021). Sensitivity of six typical spatiotemporal fusion methods to different influential factors: A comparative study for a normalized difference vegetation index time series reconstruction. *Remote Sensing of Environment, 252*

Zhu, L., Webb, G.I., Yebra, M., Scortechini, G., Miller, L., & Petitjean, F. (2021). Live fuel moisture content estimation from MODIS: A deep learning approach. *Isprs Journal of Photogrammetry and Remote Sensing, 179*, 81-91